ISSN 2409-5613 (print)
ISSN 2411-1414 (online)

# Chimica Techno Acta

2017. Vol. 4. N 4

cta.urfu.ru

Founded by Ural Federal University named after the first President of Russia B. N. Yeltsin
19, Mira St., Ekaterinburg, 620002, Russia


Учредитель – Уральский федеральный университет имени первого Президента России Б. Н. Ельцина
620002, Россия, Екатеринбург, ул. Мира, 19

Chimica Techno Acta

2017 | Vol. 4 | № 4

Scientific and Technical Journal
Established in 2014
Published four times per year

Chimica Techno Acta


Chimica Techno Acta

2017 | Vol. 4 | № 4

Научно-технический журнал
Журнал основан в 2014 г.
Выходит четыре раза в год

*Chimica Techno Acta*

# Graphical Abstracts

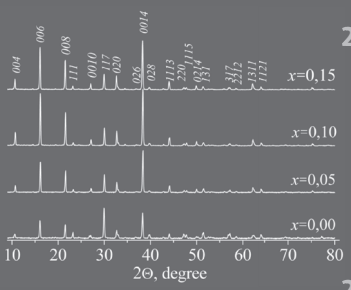




Klyndyuk A.I., Chizhova E.A., Poznyak A.I.
Preparation and characterization of $Bi_{4-x}Pr_xTi_3O_{12}$ solid solutions

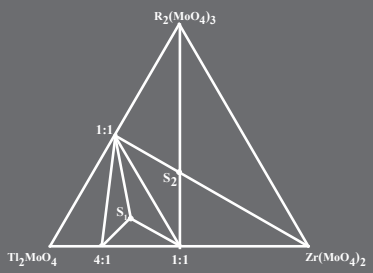




Grossman V.G., Bazarov B.G., Bazarov Zh.G.
Phase equilibria in the $Tl_2MoO_4$–$R_2(MoO_4)_3$–$Zr(MoO_4)_2$ (R = Al, Cr) systems: synthesis, structure and properties of new triple molybdates $Tl_5RZr(MoO_4)_6$ and $TlRZr_{0.5}(MoO_4)_3$

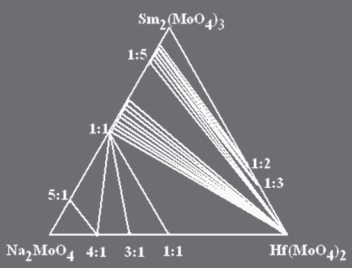




Bazarova Zh. G., Grossman V. G., Bazarov B. G., Tushinova Yu. L., Chimitova O. D., Bazarova Ts. T.
Phase diagrams for the $M_2MoO_4$–$Ln_2(MoO_4)_3$–$Hf(MoO_4)_2$ systems, where M = Li–Cs, Tl and Ln = La–Lu

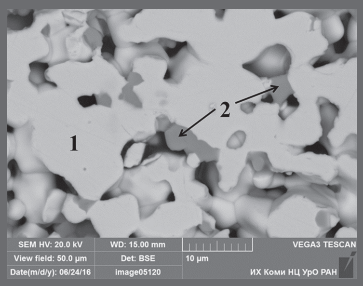




Koroleva M.S., Piir I.V., Istomina E.I.
Synthesis, structure and electrical properties of Mg-, Ni-codoped bismuth niobates



# CONTENTS/СОДЕРЖАНИЕ

Klyndyuk A.I., Chizhova E.A., Poznyak A.I.
Chimica Techno Acta. 2017. Vol. 4, No. 4. P. 210–217.
ISSN 2409–5613

DOI: 10.15826/chimtech/2017.4.4.01

**A.I. Klyndyuk, E.A. Chizhova, A.I. Poznyak**

*Belarus State Technological University*
*13a Sverdlova St., Minsk, 220006, Republic of Belarus*

# Preparation and characterization of $Bi_{4-x}Pr_xTi_3O_{12}$ solid solutions

The $Bi_{4-x}Pr_xTi_3O_{12}$ (BPT) solid solutions ($x$ = 0.05, 0.10, 0.15) with small praseodymium content were prepared by solid-state method. Thermal, electric, and dielectric properties of BPT were studied. It was revealed that BPT titanates crystalize in an orthorhombic structure and exhibit $p$-type semiconductivity. Dielectric constant of BPT increased, Curie temperature ($T_C$), electrical conductivity and dielectric losses decreased, but lattice parameters and thermo-EMF coefficient remained practically unchanged with the increase of praseodymium content in layered $Bi_{4-x}Pr_xTi_3O_{12}$. It was determined that activation energy of direct current (DC) electrical conductivity and linear thermal expansion coefficient (LTEC) of BPT changes at ferroelectric (FE) → paraelectric (PE) phase transition. The activation energy and LTEC changed below and above $T_C$ from 1.08–1.56 eV to 0.45–0.86 eV and from $(9.10–10.80)\cdot10^{-6}$ $K^{-1}$ to $(13.12–14.61)\cdot10^{-6}$ $K^{-1}$, respectively. The AC electrical conductivity studies of BPT illustrated short-range order with ionic translations assisted by small-polaron hopping.

**Keywords:** layered bismuth titanates; dielectric constant; dielectric losses; electrical conductivity; thermo-EMF; thermal expansion.

Received: 20.10.2017; accepted: 15.11.2017; published: 25.12.2017.



## Introduction

$Bi_4Ti_3O_{12}$ belongs to the Aurivillius phase family $Bi_2A_{n-1}B_nO_{3n+3}$, structure of which consists of alternated fluorite-like $[Bi_2O_2]^{2+}$ layeres and perovskite-like $[A_{n-1}B_nO_{3n+1}]^{2-}$ blocks, where $n$ – number of octahedral layers in the perovskite-like block [1]. This triple-layered ($n$ = 3) Aurivillius phase is ferroelectric with high Curie temperature ($T_C$ = 948 K [2]). The possibility to preserve the ferroelectric properties within a wide temperature range lets us to consider layered bismuth titanate as a promising material for radio-, acusto-, and optoelectronics; and thus can be used for production of optical displays, piezoelectric transducers, filters, capacitors, and different types of memory devices. So, for example, as a material for non-volatile memory devices the lanthanum-substituted $Bi_{3.25}La_{0.75}Ti_3O_{12}$ bismuth titanate is proposed, functional characteristics of which are better than of traditional ferroelectrics, such as $PbTi_{1-x}Zr_xO_3$ or $SrBi_2Ta_2O_9$ [3].

Crystal structure, physico-chemical, and functional properties of the solid solutions $Bi_{4-x}Ln_xTi_3O_{12}$ (Ln = rare-earth element) were studied in a number of pa-

pers [1, 3–8]. In [4] it was found that partial substitution of Bi by La in $Bi_4Ti_3O_{12}$ leads to decrease of orthorhombic distortion degree of $Bi_{4-x}La_xTi_3O_{12}$ solid solutions at $x \le 1.0$, and at $x > 1.0$ they had tetragonal structure and were paraelectrics. According to the [1, 4] results, at $x \le 0.75$ $La^{3+}$ ions substitute $Bi^{3+}$ in perovskite-like $[Bi_2Ti_3O_{10}]^{2-}$ blocks, and at $x > 0.75$ they can substitute $Bi^{3+}$ ions in fluorite-like $[Bi_2O_2]^{2+}$ layers too, so formula of $Bi_{4-x}La_xTi_3O_{12}$ solid solutions at $x \le 0.75$ and $x > 0.75$ should be written as $[Bi_2O_2][Bi_{2-x}La_xTi_3O_{10}]$ and $[Bi_{2-y}La_yO_2][Bi_{2-x+y}La_{x-y}Ti_3O_{10}]$, respectively. Authors of [5] established that partial substitution of Bi with La or Ce in $Bi_4Ti_3O_{12}$ leads to the decrease of Curie temperature of ceramics ($T_C$ values for $Bi_{3.5}La_{0.5}Ti_3O_{12}$ and $Bi_{3.5}Ce_{0.5}Ti_3O_{12}$ samples were 798 and 813 K, respectively, both being lower than $T_C$ for $Bi_4Ti_3O_{12}$ phase). At the same time, $La_2O_3$ addition to the layered bismuth titanate improved its dielectric properties; by authors' opinion, it was caused by decreasing of oxygen vacancy concentration in ceramics. Partial substitution of Bi with Nd in $Bi_4Ti_3O_{12}$ leads to the decrease of Curie temperature, dielectric losses, and electrical conductivity of $Bi_{4-x}Nd_xTi_3O_{12}$ ceramic; and impoves its polarization properties because of reduction of bismuth and oxygen vacancy concentrations [7]. In [8] the $Bi_{4-y}Tb_yTi_3O_{12}$ phase formation in the powder mixtures of $Bi_2O_3$, $Tb_4O_7$, and $TiO_2$ was investigated. It was found that partial replacing of Bi by Tb results in shrinking of unit cell of $Bi_{4-y}Tb_yTi_3O_{12}$ solid solutions, decrease of orthorhombic distortion degree of their crystal lattice, and, as a consequence, leads to the decrease of temperature of FE → PE (ferroelectric → paraelectric) phase transition (up to ≈28 K for $y = 0.4$).

In this work the results of investigation of crystal structure, thermal, electric, and dielectric properties of ceramic samples of $Bi_{4-x}Pr_xTi_3O_{12}$ (BPT) solid solutions with small praseodymium oxide content ($x \le 3.75$ mol.%) are presented.

## Experimental

$Bi_{4-x}Pr_xTi_3O_{12}$ ($x$ = 0.00, 0.05, 0.10, 0.15) ceramic samples were prepared by solid-state reactions method from mixtures of $Bi_2O_3$ (99.0%), $Pr_6O_{11}$ (99.0%), and $TiO_2$ (99.5%) powders taken in appropriate stoichiometric ratios. Precursor mixtures were calcuned in air within temperature interval of 923–1223 K for 17 hours with some intermediate regrindings, according to procedure described in details in [6].

Identification of the samples was performed using X-ray diffraction analysis (XRD) (Bruker D8 XRD Advance diffractometer, Cu Kα radiation) and IR absorption spectroscopy (IR Fourier-spectrometer Nexus of ThermoNicolet). Relative density ($\rho_{rel}$) of the samples was calculated as

$$\rho_{rel} = (\rho_{app}/\rho_{XRD}) \cdot 100\%, \quad (1)$$

where $\rho_{app}$ – apparent density, determined from the mass and dimensions of the samples; $\rho_{XRD}$ – X-ray density.

Thermal expansion of the samples was studied using DIL 402 PC (Netzsch) dilatometer within 290–1130 K with heating-cooling rate of 1–5 K/min. Dielectric measurements were carried out in the temperature range 300–1090 K for frequencies between 100 Hz and 1 MHz using immittance meter E7–25. DC electrical conductivy and thermo-EMF of sintered ceramics were studied within the temperature ranges of 470–1090 K and 780–1090 K,

respectively, according to the procedure described elsewhere [9]. Values of linear thermal expansion coefficient (LTEC, α) and activation energy of DC electrical conductivity ($E_A$) of the samples were determined from linear parts of $\Delta l/l_0 = f(T)$, and $\lg\sigma_{DC} = f(1/T)$ dependences, respectively. All measurements were performed in air.

## Results and discussion

All $Bi_{4-x}Pr_xTi_3O_{12}$ samples after final stage of annealing were found single phase within XRD reliability (Fig. 1), and crystallized in orthorhombic structure like parent compound $Bi_4Ti_3O_{12}$ (space group *B*2*cb*) [10]. Lattice constants of $Bi_4TiO_{12}$ ($a$ = 5.449(9) Å, $b$ = 5.422(9) Å, and $c$ = 32.85(4) Å) were in a close agreement with an earlier studies: 5.444(1), 5.413(1), and 32.858(1) Å [10], 5.4403, 5.4175, and 32.7862 Å [11], and 5.4438(1), 5.4105(1), and 32.8226(5) Å [8]. Lattice constants of $Bi_{4-x}Pr_xTi_3O_{12}$ solid solutions were close to the $Bi_4Ti_3O_{12}$ ones (for example, for $Bi_{3.90}Pr_{0.10}Ti_3O_{12}$ $a$ = 5.449(7) Å, $b$ = 5.420(9) Å, and $c$ = 32.80(3) Å), which agrees with the fact that sizes of substituting and substituted ions are close to each other (for C.N. = 6 according to [12] $Bi^{3+}$ and $Pr^{3+}$ ionic radii are 1.11 and 1.013 Å, respectively).

It should be noted that 0014 reflection in the $Bi_{4-x}Pr_xTi_3O_{12}$ diffractograms was the most intensive, in contrast with 117 peak for $Bi_4Ti_3O_{12}$. Other 00l peaks had higher intensity as well ($I_{006}/I_{117}$ ratio was equal to 0.6, 1.7, 3.0, and 2.8 for $x$ = 0.00, 0.05, 0.10, and 0.15, respectively). This fact shows that partial substitution of Bi with Pr in $Bi_4Ti_3O_{12}$ leads to the texturing of the samples. The nature of this phenomenon is not clear yet and will be studied in the future.

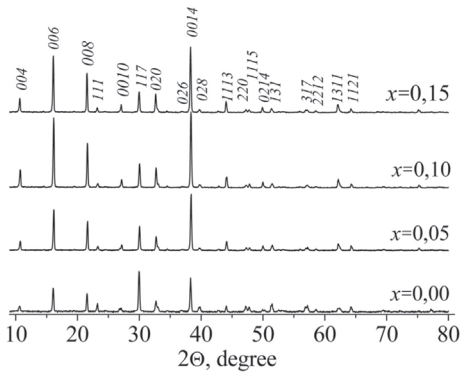


Fig. 1. X-ray powder diffractograms (Cu Kα radiation) of $Bi_{4-x}Pr_xTi_3O_{12}$ solid solutions

Three absorption bands occurring at 810–818 $cm^{-1}$ ($\nu_1$), 573–582 $cm^{-1}$ ($\nu_2$), and 474 $cm^{-1}$ ($\nu_3$) were observed in the absorption spectra of $Bi_{4-x}Pr_xTi_3O_{12}$ powders. According to [7, 11], these bands correspond to the stretching ($\nu_1$ and $\nu_2$) and bending ($\nu_3$) vibrations of Bi–O ($\nu_1$ and $\nu_3$) and Ti–O ($\nu_2$) bonds, respectively. The peak positions did not change with $x$ increasing, so partial replacing of Bi by Pr in layered $Bi_4Ti_3O_{12}$ did not affect practically the metal-oxygen interactions in its crystal structure.

The relative density values for $Bi_{4-x}Pr_xTi_3O_{12}$ ceramics varied within 77–80% and increased with $x$, being essentially larger than for unsubstituted bismuth titanate (60%). These results show that addition of praseodymium oxide to the layered bismuth titanate improves its sinterability. Note that according to the literature data [6, 7] addition of lanthanum or neodymium oxides to the $Bi_4Ti_3O_{12}$, on the contrary, had lowered its sinterability.

On the temperature dependences of relative elongation an inflection point near 940–970 K was observed (Fig. 2). It is related to the FE → PE phase transition [8] and is accompanied by the increase of LTEC values of the samples (Table 1).

An inflection point, which was determined as an intersection of linear parts of $\Delta l/l_0 = f(T)$ dependences at low (FE region) and high temperatures (PE region), corresponds to the Curie temperature and decreases with $x$ (Fig. 2, inset). It is in a good agreement with the literature data, according to which substitution of Bi with Ln in $Bi_4Ti_3O_{12}$ leads to lowering of its Curie temperature [4–8].

The LTEC values of $Bi_{4-x}Pr_xTi_3O_{12}$ titanates in FE state decreased, but in PE state increased with $x$ (Table 1). The LTEC values in PE state can be explaned by anharmonicity of metal-oxygen vibrations in disordered cationic sublattice of $Pr^{3+}$-substituted bismuth titanate $Bi_{4-x}Pr_xTi_3O_{12}$. The LTEC values in FE state could be caused either by increase of dipole-dipole interactions or by decrease of oxygen and bismuth vacancy concentrations in the BPT. The first explanation is in contrast with the fact that $T_C$ of $Bi_{4-x}Pr_xTi_3O_{12}$ solid solutions decreases with $x$. So, the decrease of LTEC values of BPT ceramics in FE region is due to the decrease of the vacancy concentration in it [3].

$Bi_{4-x}Pr_xTi_3O_{12}$ compounds are $p$-type semiconductors (Fig. 3), which confirms previous data [7, 14]. According to [7, 14] electrical conductivity of layered bismuth titanate increases with temperature [7,14] and thermo-EMF coefficient of $Bi_4Ti_3O_{12}$ phase at high temperatures is positive [14]. Seebeck coefficient values of BPT ceramics were close to each other (Fig. 3b), which corresponds to the isovalent character of substitution of Bi with Pr. But DC electrical conductivity of the samples decreased with $x$ (Fig. 3a) due to the defect concentration decrease as was mentioned above. Near $T_C$ there is a change in the slope of linear sections at the Arrhenius plots $\lg\sigma_{DC} = f(1/T)$. Values of activation energy of the samples' DC electrical conductivity in PE region are essentially less than in FE one (Table 1). Similar results were obtained in [15] for $Bi_4Ti_2Nb_{0.5}Fe_{0.5}O_{12}$ ceramics, activation energy values of which were equal to 1.21 eV and 0.50 eV below and above $T_C$, respectively (AC, $\omega = 10^5$ Hz). Partial substitution of Bi with Pr in $Bi_4Ti_3O_{12}$ increases $E_A$ of BPT in FE state and low-

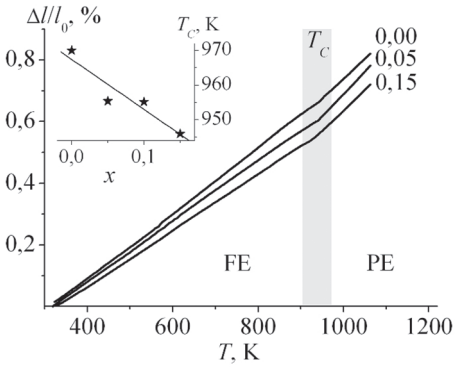


Fig. 2. Temperature dependences of relative elongation of $Bi_{4-x}Pr_xTi_3O_{12}$ sintered ceramics. Inset shows concentration dependences of $T_C$

Table 1

Values of apparent activation energy of DC electrical conductivity ($E_A$) and linear thermal expansion coefficient (α) of $Bi_{4-x}Pr_xTi_3O_{12}$ titanates

| $x$ | $E_A$, eV | | α·10⁶, K⁻¹ | |
|---|---|---|---|---|
| | FE | PE | FE | PE |
| 0.00 | 1.08±0.02 | 0.86±0.02 | 10.80±0.06 | 13.12±0.02 |
| 0.05 | 1.24±0.01 | 0.46±0.02 | 09.62±0.01 | 14.61±0.02 |
| 0.10 | 1.23±0.02 | 0.45±0.01 | 09.31±0.01 | 13.53±0.01 |
| 0.15 | 1.56±0.04 | 0.49±0.01 | 09.10±0.01 | 13.48±0.01 |

ers it in PE state (Table 1). Note that $E_A$ value of layered bismuth titanate below $T_C$ obtained in this work coincides with the data given in [14]: 1.0 eV for $Bi_4Ti_3O_{12}$ ceramics.

In the temperature dependences of dielectric constant of $Bi_{4-x}Pr_xTi_3O_{12}$ titanates abrupt maxima near 930–940 K was observed (Fig. 4a). It was caused by FE → PE phase transition, and phase transition temperature ($T_C$) lowered with increasing praseodymium content in the samples (Fig. 4d) and was close to the $T_C$ values determined from the $\Delta l/l_0 = f(T)$ dependences (Fig. 2, inset). Dielectric constant values of BPT ceramics increased with $x$, which was more prominent at high temperatures (Fig. 4a, c). Dielectric losses of investigated samples increased with temperature and decreased when Pr concentration (Fig. 4b, e). Besides, on the tgδ = $f(T)$ dependences two anomalous regions were observed: near 760–820 K and 930–940 K. The second anomaly is related to the FE → PE phase transition, but the first one is probably due to the oxygen vacancy movement out (migration) of the domain walls [16].

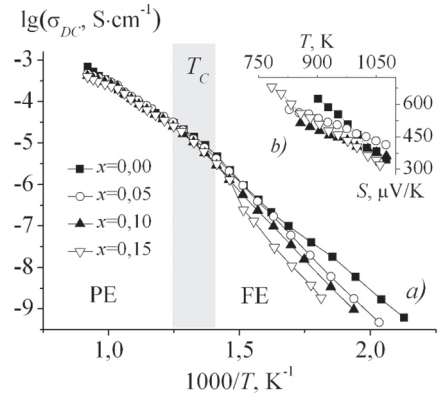


Fig. 3. Dependences of DC electrical conductivity (*a*) and thermo-EMF coefficient (*b*) of $Bi_{4-x}Pr_xTi_3O_{12}$ samples vs temperature

The values of Curie temperature of the samples are frequency independent (Fig. 5*a*, *b*), which indicates that $Bi_{4-x}Pr_xTi_3O_{12}$ phases are normal ferroelectrics [15]. When the testing frequency increased from 100 Hz to 100 kHz, the dielectric constant and dielectric losses of BPT ceramics decreased substantially due to the suppression of relaxing polarization at high frequencies.

The dielectric constant of normal ferroelectrics follows the Curie–Weiss law

$$\varepsilon = C/(T - T_\Theta), \qquad (2)$$

where $C$ is Curie–Weiss constant and $T_\Theta$ is Curie–Weiss temperature. The Curie–

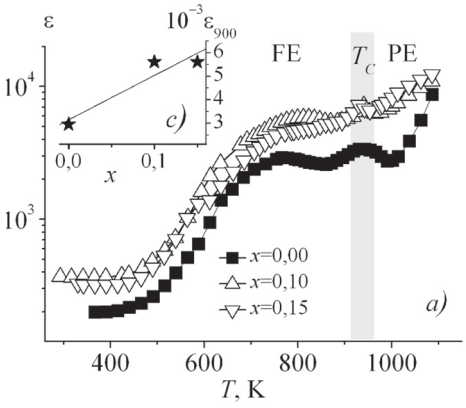


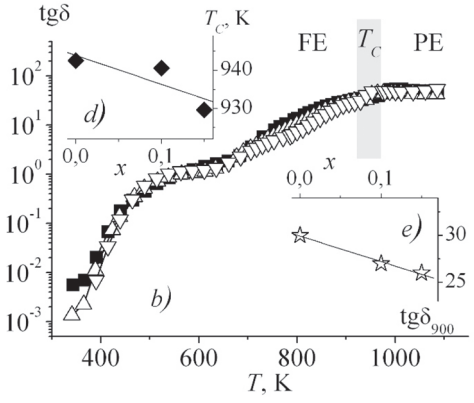


Fig. 4. Temperature (a, b) and concentration (c–e) dependences of dielectric constant (a, c), dielectric losses (b, e), and $T_C$ (*d*) of $Bi_{4-x}Pr_xTi_3O_{12}$ ceramics (ω = 1 kHz)

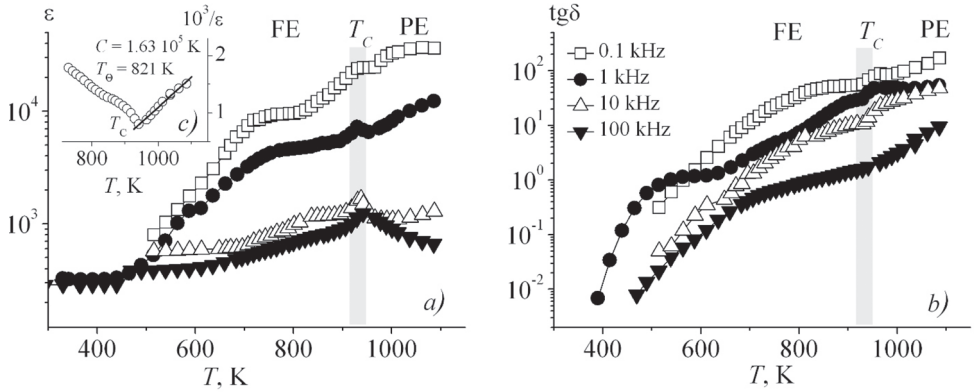


Fig. 5. Temperature dependences of dielectric constant (a) and dielectric losses (b) of $Bi_{3.85}Pr_{0.15}Ti_3O_{12}$ at different frequencies. Inset (c) shows the inverse dielectric constant as a function of temperature at 100 kHz

Weiss plot for $Bi_{3.85}Pr_{0.15}Ti_3O_{12}$ phase at 100 kHz is shown in the Fig. 5c. The parameters obtained from the linear fit are $C = 1.63\times10^5$ K and $T_\Theta = 821$ K. The magnitude of Curie–Weiss constant is of the same order as of well-known displasive-type ferroelectrics, such as $BaTiO_3$ ($C = 1.7\cdot10^5$ K [15]).

The frequency dependences of AC electrical conductivity of $Bi_{3.85}Pr_{0.15}Ti_3O_{12}$ at various temperatures are given in Fig. 6. The frequency independent plateau at low frequencies is attributed to the long-range translational motion of ions contributing to DC conductivity ($\sigma_{DC}$) [17, 18]. At high frequencies (>$10^4$ Hz) the AC electrical conductivity shows $\omega^n$ dependence which corresponds to the short-range translation ion hopping [15, 18].

The frequency dependent AC electrical conductivity of BPT ceramics obeys Jonscher's power law [19] at all temperatures

$$\sigma(\omega) = \sigma(0) + A\omega^n, \qquad (3)$$

where $\sigma(\omega)$ is the total conductivity, $\sigma(0)$ is the DC conductivity, $A$ is the temperature-dependent constant which determines the strength of polarizability, and $n$ represents the degree of interaction between the mobile ions and the lattice around them [15, 19]. The values of $n$ are less than one, which indicates that motion of charge carriers is translational [18, 20]. The shape of $n$ vs. $T$ dependence suggests hopping mechanisms of charge carriers [18, 19]. In case of small-polaron hopping, $n$ increases with temperature, while for a large polaron hopping, $n$ decreases with temperature. As shown in inset of Fig. 6, the values of $n$ are less than 1 and are found to increase with temperature;

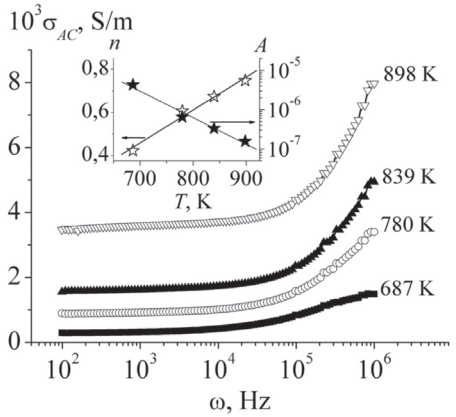


Fig. 6. Frequency dependences of AC electrical conductivity of $Bi_{3.85}Pr_{0.15}Ti_3O_{12}$ at different temperatures. Inset shows the variation of Jonscher's power law parameters ($n$, $A$) as a function of temperature

hence we conclude that AC electrical conductivity arises mainly due to the short-range order translation hopping assisted by small-polaron hopping mechanism.

## Conclusions

The $Bi_{4-x}Pr_xTi_3O_{12}$ solid solutions ($x$ = 0.05, 0.10, 0.15) with small substitution degree were synthesized and their thermal expansion, DC and AC electrical conductivity, dielectric constant and dielectric losses were measured. The samples crystallized in orthorhombic structure and possessed *p*-type semiconductive and normal ferroelectric properties. Lattice constants and thermo-EMF coefficient of BPT were practically composition independent, but Curie temperature, electrical conductivity and dielectric losses decreased with $x$. Activation energy of DC electrical conductivity and linear thermal expansion coefficient of $Bi_{4-x}Pr_xTi_3O_{12}$ changed at the temperature of ferroelectric to paraelectric phase transition, and their values were 1.08–1.56 eV and 0.45–0.86 eV, and $(9.10–10.80)\cdot10^{-6}$ $K^{-1}$ and $(13.12–14.61)\cdot10^{-6}$ $K^{-1}$ below and above Curie temperature, respectively. AC electrical conductivity investigations illustrate short-range order ionic translation hopping assisted by small-polaron hopping mechanism.


## Acknowledgements

This work was carried out within the framework of State Program of Scientific Investigations of Belarus Republic «Physical materials science, new materials and technologies» (subprogram «Materials science and technologies of materials», task 1.17).


## References


1. Hyatt NC, Hriljac JA, Comyn TP. Cation disorder in $Bi_2Ln_2Ti_3O_{12}$ Aurivillius phases (*Ln* = La, Pr, Nd and Sm). *Mat Res Bull*. 2003;38:837–46. DOI:10.1016/S0025–5408(03)00032–1.
2. Scott JF, Araujo CA. Ferroelectric memories. *Science*. 1989;246(4936):1400–5. DOI:10.1126/science.246.4936.1400.
3. Park BH, Kang BS, Bu SD, Noh TW, Lee J, Jo W. Lanthanum-substituted bismuth titanate for use in non-volatile memories. *Nature*. 1999;401:682–4. DOI:10.1038/44352.
4. Wu D, Yang B, Li A. Structural phase transition due to La substitution in $Bi_4Ti_3O_{12}$. *Phase Transitions*. 2009;82(2):146–55. DOI:10.1080/01411590802524992.
5. Pavlović N, Koval V, Dusza J, Srdić VV. Effect of Ce and La substitution on dielectric properties of bismuth titanate ceramics. *Ceram Int*. 2011;37:487–92. DOI:10.1016/j.ceramint.2010.09.005.
6. Klyndyuk AI, Glinskaya AA, Chizhova EA, Bashkirov LA. Synthesis and properties of lanthanum-substituted bismuth titanate with structure of Aurivillius phase. *Refractories & Technical Ceramics*. 2017;(1–2):29–33. Russian.
7. Kan YM, Zhang GJ, Wang PL, Cheng YB. Preparation and properties of neodymium-modified bismuth titanate ceramics. *J Eur Ceram Soc*. 2008;28:1641–7. DOI:10.1016/j.jeurceramsoc.2007.10.010.

8. Fortalnova EA, Politova ED, Ivanov SA, Safronenko MG. Phase formation and physicochemical properties of solid solutions $Bi_{4-y}Tb_yTi_3O_{12}$ based on layered bismuth titanate. *Russ J Inorg Chem*. 2017;62(2):224–30. DOI:10.1134/S0036023617020061.
9. Klyndyuk AI, Chizhova EA. Structure, Thermal Expansion, and Electrical Properties of $BiFeO_3$–$NdMnO_3$ Solid Solutions. *Inorg Mater*. 2015;51(3):272–7. DOI:10.1134/S0020168515020090.
10. Villegas M, Jardiel T, Caballero AC, Fernandez JF. Electrical Properties of Bismuth Titanate Based Ceramics with Secondary Phases. *J Electroceram*. 2004;13:543–8. DOI:10.1007/s10832–004–5155–2.
11. Stojanović BD, Simoes AZ, Paiva-Santos CO, Quinelato C, Longo E, Varela JA. Effect of processing route on the phase formation and properties of $Bi_4Ti_3O_{12}$ ceramics. *Ceram Int*. 2006;32:707–12. DOI:10.1016/j.ceramint.2005.05.007.
12. Shannon RD. Revised effective ionic radii and systematic studies of interatomic distances in halides and chalcogenides. *Acta Cryst*. 1976; A32:751–67. DOI:10.1107/S0567739476001551.
13. Chen Z, Yu Y, Hu J, Shui A, He X. Hydrothermal synthesis and characterization of $Bi_4Ti_3O_{12}$ powders. *J Ceram Soc Jap*. 2009;117(3):264–7. DOI:10.2109/jcersj2.117.264.
14. Kim SK, Miyayama M, Yanagida H. Electrical anisotropy and a plausible explanation for dielectric anomaly of $Bi_4Ti_3O_{12}$ single crystal. *Mat Res Bull*. 1996;31(1):121–31. DOI:10.1016/0025–5408(95)00161–1.
15. Kumar S, Varma KBR. Structural and dielectric properties of $Bi_4Ti_2Nb_{0.5}Fe_{0.5}O_{12}$ ceramics. *Solid State Commun*. 2008;146:137–42. DOI:10.1016/j.ssc.2008.02.004.
16. Jimenez B, Jimenez R, Castro A, Millan P, Pardo L. Dielectric and mechanoelastic relaxations due to point defects in layered bismuth titanate ceramics. *J Phys: Condens Matter*. 2001;13(33):7315–26. DOI:10.1088/0953–8984/13/33/312.
17. Shashkov MS, Malyshkina OV, Piir IV, Koroleva MS. Dielectric properties of iron-containing bismuth titanate solid solutions with a layer perovskite structure. *Phys Solid State*. 2015;57(3):518–21. DOI:10.1134/S1063783415030312.
18. Kumari S, Ortega N, Kumar A, Pavunny SP, Hubbard JW, Rinaldi C, Srinivasan G, Scott JF, Katiyar RS. Dielectric anomalies due to grain boundary conduction in chemically substituted $BiFeO_3$. *J Appl Phys*. 2015;117:114102. DOI:10.1063/1.4915110.
19. Jonscher AK. The 'universal' dielectric response. *Nature*. 1977;267:673–9. DOI:10.1038/267673a0.
20. Sadykov SA, Palchaev DK, Murlieva ZK, Alikhanov NM, Rabadanov MK, Gadzhimagomedov SK, Kallaev SN. AC conductivity of $BiFeO_3$ ceramics obtained by spark plasma sintering of nanopowders. *Phys Solid State*. 2017;59(9):1771–7. DOI:10.1134/S1063783417090268.

**Cite this article as:**
Klyndyuk AI, Chizhova EA, Poznyak AI. Preparation and characterization of $Bi_{4-x}Pr_xTi_3O_{12}$ solid solutions. *Chimica Techno Acta*. 2017;4(4):211–7. DOI:10.15826/chimtech/2017.4.4.01.

Grossman V.G., Bazarov B.G., Bazarova Zh.G.
Chimica Techno Acta. 2017. Vol. 4, No. 4. P. 218–223.
ISSN 2409–5613

DOI: 10.15826/chimtech/2017.4.4.02

**V.G. Grossman[1], B.G. Bazarov[1,2], Zh.G. Bazarova[2]**

*[1]Baikal Institute of Nature Management,*
*Siberian Branch of Russian Academy of Sciences,*
*8 Sakh'yanovoi St., Ulan-Ude, 670047, Russian Federation*
*e-mail: grossmanv@mail.ru*
*[2]Buryat State University,*
*24a SmolinaSt., Ulan-Ude, 670000, Russian Federation*

# Phase equilibria in the $Tl_2MoO_4$–$R_2(MoO_4)_3$–$Zr(MoO_4)_2$ (R = Al, Cr) systems: synthesis, structure and properties of new triple molybdates $Tl_5RZr(MoO_4)_6$ and $TlRZr_{0.5}(MoO_4)_3$

The $Tl_2MoO_4$–$R_2(MoO_4)_3$–$Zr(MoO_4)_2$ (R = Al, Cr) systems were studied in the subsolidus region using X-ray powder diffraction and differential scanning calorimetric (DSC) analysis. Quasi-binary joins were revealed, and triangulation was carried out. New ternary molybdates $Tl_5RZr(MoO_4)_6$ (5:1:2) and $TlRZr_{0.5}(MoO_4)_3$ (1:1:1) (R = Al, Cr) were prepared. The unit cell parameters for the new compounds were calculated.

**Keywords:** phase equilibria, synthesis, systems, thallium, zirconium, iron, aluminum, crystal structure, space group.

Received: 23.10.2017; accepted: 01.12.2017; published: 25.12.2017.



## Introduction

This paper is a continuation of our systematic studies of phase relations in the $Tl_2MoO_4$–$R_2(MoO_4)_3$–$A(MoO_4)_2$ (R – trivalent metals, A = Zr, Hf) ternary salt systems [1]. Earlier we studied phase equilibria in the $Tl_2MoO_4$–$Fe_2(MoO_4)_3$–$Hf(MoO_4)_2$ system [2]. Subsolidus phase diagrams for this system and constituent double systems were constructed, and triple molybdates $Tl_5FeHf(MoO_4)_6$ and $TlFeHf_{0.5}(MoO_4)_3$ had been detected. The aims of the present study include (1) investigation of phase equilibria in the ternary salt systems $Tl_2MoO_4$–$R_2(MoO_4)_3$–$Zr(MoO_4)_2$ (R = Al, Cr), (2) determination of optimal condition for the solid state synthesis of ternary molybdates found in these systems, and (3) determination of crystallographic and thermal characteristics of the obtained compounds.

## Experimental

Subsolidus phase relations in the $Tl_2MoO_4$–$R_2(MoO_4)_3$–$Zr(MoO_4)_2$ (R = Al, Cr) systems were studied in the subsolidus region (500–550 °C) using the intersecting joins method.

The corresponding molybdates of thallium, aluminum, chromium and zirconium were used as initial components for studying the phase equilibria in the $Tl_2MoO_4$–$R_2(MoO_4)_3$–$Zr(MoO_4)_2$ (R = Al,

Cr) systems. Synthesis of $Tl_2MoO_4$ was carried out according to the reaction $Tl_2O_3+MoO_3 \rightarrow Tl_2MoO_4+O_2\uparrow$ at gradually increasing temperature in the range 400–550 °C for 50 h. The high temperature modification of $Zr(MoO_4)_2$ was prepared by annealing of stoichiometric mixture of binary oxides $ZrO_2$ and $MoO_3$ at 400–700 °C for 100 h. Aluminum molybdate and chromium molybdate were obtained by calcination of stoichiometric mixtures of precursors $Al(NO_3)_3 \cdot 9H_2O$, $Cr_2O_3$, and $MoO_3$ in the temperature range 400–650 °C for 100 h. The initial stage of each synthesis was chosen as 400 °C since $MoO_3$ possesses high volatility at temperature about 600 °C. To ensure better homogenization, the reaction mixtures were ground in ethanol every 20–30 h during firing. After annealing, the samples were slowly cooled in the furnace. The non-equilibrium samples were additionally annealed. It was assumed that equilibrium is reached if the phase composition of the samples remains unchanged during two consecutive anneals. The crystallographic parameters of the synthesized compounds were close to those reported in literature [3–5].

X-ray powder diffraction (XRD) measurements were performed using Bruker D8 Advance diffractometer (Bragg–Brentano geometry, Cu Kα radiation, secondary monochromator, maximum angle $2\theta=100°$, scan step 0.02°). The differential scanning calorimetric (DSC) analysis of the samples was carried out using NETZCH STA 449C (Jupiter, Germany) thermoanalyzer. Compounds' pellets were placed in a Pt-crucible, heated up and then cooled down in argon atmosphere with the heating and cooling rate of 10 K/min.

## Results and discussion

The information about the phase formation in the $Tl_2MoO_4$–$R_2(MoO_4)_3$–$Zr(MoO_4)_2$ (R = Al, Cr) systems, which represent the bounding sides of the studied system, were taken from previous papers [3–5]. The formation of double molybdates with general composition $TlR(MoO_4)_2$ was detected in the boundary $Tl_2MoO_4$–$R_2(MoO_4)_3$ systems [3]. Two double molybdates $Tl_8Zr(MoO_4)_6$ and $Tl_2Zr(MoO_4)_3$ were formed in the $Tl_2MoO_4$–$Zr(MoO_4)_2$ system [4]. No intermediate compounds were found in the $R_2(MoO_4)_3$–$Zr(MoO_4)_2$ systems [5].

In order to find new triple molybdates, the subsolidus phase equilibria in the $Tl_2MoO_4$–$R_2(MoO_4)_3$–$Zr(MoO_4)_2$ (R = Al, Cr) systems were studied at 500–550 °C and its triangulated phase diagrams were constructed. Solid-state interactions between $Tl_2MoO_4$, $R_2(MoO_4)_3$, and $Zr(MoO_4)_2$, which occurred over wide ranges of temperature and concentration, led to the formation of new triple molybdates $Tl_5RZr(MoO_4)_6$ (5:1:2 mole ratio) $S_1$ and $TlRZr_{0.5}(MoO_4)_3$ (1:1:1 mole ratio) $S_2$. Compound $S_2$ was found at the intersection point of the $R_2(MoO_4)_3$–$Tl_2Zr(MoO_4)_3$ and $TlR(MoO_4)_2$–$Zr(MoO_4)_2$ joins. The triple molybdate ($S_1$) locates inside the triangle with the double molybdates $TlR(MoO_4)_2$, $Tl_8Zr(MoO_4)_6$ and $Tl_2Zr(MoO_4)_3$ in its vertices.

The phase relations in the $Tl_2MoO_4$–$R_2(MoO_4)_3$–$Zr(MoO_4)_2$ (R = Al, Cr) systems are shown in Fig. 1.

Individual $Tl_5RZr(MoO_4)_6$ (R = Al, Cr) oxides were prepared by firing at 450–550 °C for 150–200 h, and the molybdates $TlRZr_{0.5}(MoO_4)_3$ (R = Al, Cr) were obtained by firing at temperatures from 500 to 600 °C for 100–150 h.

The single phase $Tl_5AlZr(MoO_4)_6$ was not synthesized under the conditions of our experiment.

The analysis of X-ray diffraction patterns of the compounds obtained shows that the reflection positions and their intensity ratio for $TlRZr_{0.5}(MoO_4)_3$ and $Tl_5RZr(MoO_4)_6$ (R = Al, Cr) are similar to $TlFeHf_{0.5}(MoO_4)_3$ [2] and $Rb_5ErHf(MoO_4)_6$ [6], respectively. It could be concluded that $TlRZr_{0.5}(MoO_4)_3$ is isostructural to $TlFeHf_{0.5}(MoO_4)_3$ and $Tl_5RZr(MoO_4)_6$ is isostructural to $Rb_5ErHf(MoO_4)_6$.

Three dimensional framework of the $TlFeHf_{0.5}(MoO_4)_3$ crystal structure ($a$ = $b$ = 13.0324(2) Å, $c$ = 11.8083(3) Å, $V$ = 1736.87(6) Å$^3$, $\rho_{calc}$=4.757 g/cm$^3$, space group $R\bar{3}$, $Z$ = 6) is composed of the Mo-tetrahedra sharing O vertices with the (Fe, Hf)$O_6$ octahedra, with thallium atoms occupying wide channels in the framework [2] (Figs. 2 and 3). The arrangement of Tl atoms (pink spheres) in the structural channel in $TlFeHf_{0.5}(MoO_4)_3$ is shown in Fig. 3.

$Rb_5ErHf(MoO_4)_6$ possesses the trigonal crystal structure: $a$ = 10.7511(1) Å, $c$ = 38.6543(7) Å, $V$ = 3869.31(9) Å$^3$, $\rho_{calc}$=4.462 g/cm$^3$, $Z$ = 6, space group $R\bar{3}c$ [6]. The three-dimensional framework of the structure is formed of the $MoO_4$ tetrahedra, which are sharing corners with two $ErO_6$ and $HfO_6$ octahedra (Fig. 4). Two types of Rb atoms occupy large cavities in the framework. The particular ar-

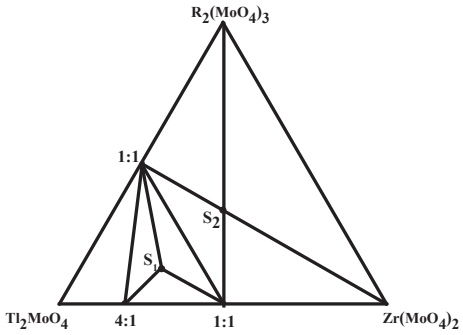


Fig. 1. Subsolidus phase relations in the $Tl_2MoO_4$–$R_2(MoO_4)_3$–$Zr(MoO_4)_2$ (R = Al, Cr) systems: $S_1$ –$Tl_5RZr(MoO_4)_6$ (5:1:2 mole ratio) and $S_2$ – $TlRZr_{0.5}(MoO_4)_3$ (1:1:1 mole ratio)

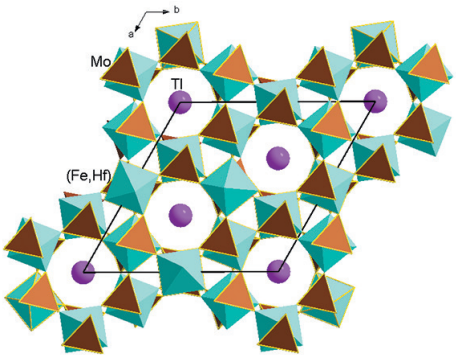


Fig. 2. The framework of $TlFeHf_{0.5}(MoO_4)_3$ crystal structure that consists of $MoO_4$ tetrahedra and (Fe, Hf)$O_6$ octahedra in the projection of layer onto the (001) plane (Tl atoms are represented by pink spheres)

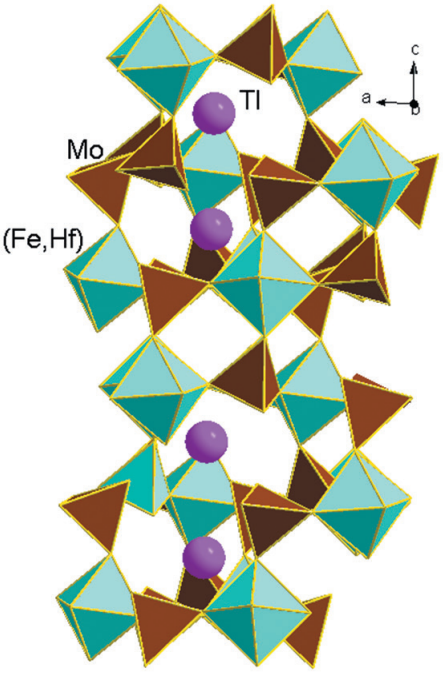


Fig. 3. The fragment of the $TlFeHf_{0.5}(MoO_4)_3$ crystal structure that is projected onto the (010) plane

rangement of Rb atoms in the structural channel is shown in Fig. 5. The distribution of the $Er^{3+}$ and $Hf^{4+}$ cations over two positions is obtained during the structure refinement.

The unit cell parameters for the synthesized triple molybdates $TlRZr_{0.5}(MoO_4)_3$ (R = Al, Cr) were refined using uniquely-indexed lines for the $TlFeHf_{0.5}(MoO_4)_3$ single crystal [2]. The lines for $Tl_5CrZr(MoO_4)_6$ were indexed using $Rb_5ErHf(MoO_4)_6$ [6] as analogous isostructural compound. The unit cell parameters that were refined using the TOPAS-4 software are listed in Table 1 along with the melting points of the corresponding compounds. Fig. 6 illustrates good coincidence of the experimental and calculated profiles.

As shown in Table 1, the unit cell parameters and volume of $TlRZr_{0.5}(MoO_4)_3$ (R = Al, Cr) and $Tl_5CrZr(MoO_4)_6$ increase with the substitution of 6-coordinated aluminum cations ($r$ = 0.535 Å) with a larger chromium cation ($r$ = 0.615 Å) [7]. The linear dependence of the unit cell volume on the trivalent element radii is also in accordance with $TlRZr_{0.5}(MoO_4)_3$ (R = Al,

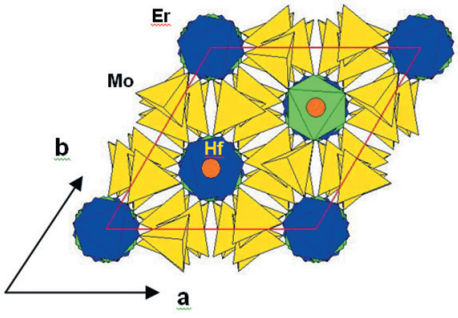


Fig. 4. Complex framework of the $Rb_5ErHf(MoO_4)_6$ crystal structure built of the $MoO_4$ tetrahedra and $(Er, Hf)O_6$ octahedra. Red parallelogram shows the projection of a layer onto the (001) plane. The Rb atoms are represented by the orange spheres

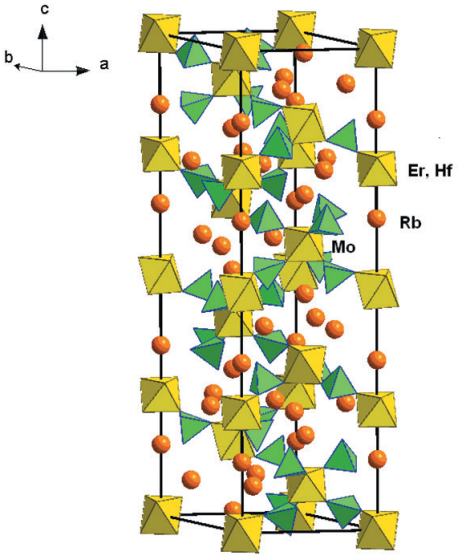


Fig. 5. Crystal structure of $Rb_5ErHf(MoO_4)_6$ as projected on plane (133)

Table 1

The unit cell parameters and melting points of $TlRZr_{0.5}(MoO_4)_3$ (R = Al, Cr) and $Tl_5CrZr(MoO_4)_6$ in comparison with literature data

| Compound | Unit cell parameters (Å) | | | | $T$, °C |
|---|---|---|---|---|---|
| | $a$, Å | $c$, Å | $V$, Å$^3$ | space group; $Z$ | |
| $TlFeHf_{0.5}(MoO_4)_3$ [2] | 13.0324(2) | 11.8083(3) | 1736.87(6) | $R\bar{3}$; 6 | 811 |
| $TlAlZr_{0.5}(MoO_4)_3$ | 12.5935(6) | 11.5946(8) | 1592.5(2) | | 751 |
| $TlCrZr_{0.5}(MoO_4)_3$ | 12.6961(6) | 11.7022(9) | 1633.6(2) | | 842 |
| $Rb_5ErHf(MoO_4)_6$ [6] | 10.7511(1) | 38.6543(7) | 3869.31(9) | $R\bar{3}c$; 6 | 730 |
| $Tl_5CrZr(MoO_4)_6$ | 10.4047(8) | 37.5322(3) | 3518.8(6) | | 599 |

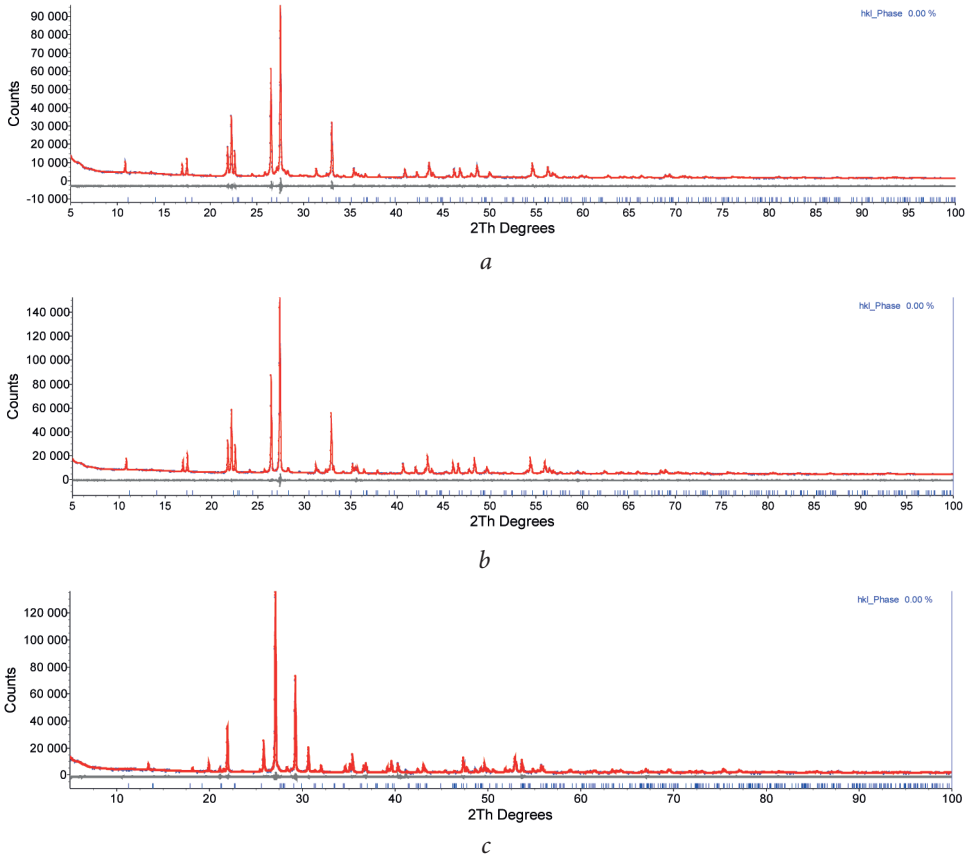


Fig. 6. Measured (red), calculated (black) and differential (blue) powder diffraction patterns for $TlCrZr_{0.5}(MoO_4)_3$ (*a*), $TlAlZr_{0.5}(MoO_4)_3$ (*b*) and $Tl_5CrZr(MoO_4)_6$ (*c*)

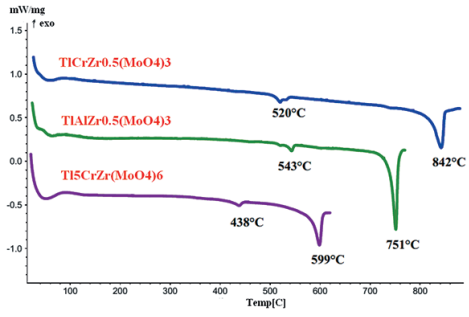


Fig. 7. DSC curves for $TlRZr_{0.5}(MoO_4)_3$ (R = Al, Cr) and $Tl_5CrZr(MoO_4)_6$

## Conclusions

New triple molybdates with general compositions $Tl_5RZr(MoO_4)_6$ (5:1:2) and $TlRZr_{0.5}(MoO_4)_3$ (1:1:1) (R = Al, Cr), respectively, were obtained in the thallium-containing systems with trivalent metals and zirconium. The formation of these triple molibdates occurs similarly to the formation of ternary molibdate $Tl(FeHf_{0.5})$ Cr) and $Tl_5CrZr(MoO_4)_6$ belonging to one structural family.

Two endothermic effects are observed on the DSC curves (Fig. 7). The first one corresponds to some structural changes that, however, are not accompanied by the change of a structural type. The last endothermic effect corresponds to the melting of the studied compounds.

$(MoO_4)_3$ in previously studied $Tl_2MoO_4$–$Fe_2(MoO_4)_3$–$Hf(MoO_4)_2$ system [2]. The phase relations do not change with hafnium ($r$ = 0.71 Å) being substituted with zirconium ($r$ = 0.72 Å) [7].


## Acknowledgements

This work was carried out according to the state assignment BINM SB RAS (project no. 0339-2016-0007).


## References


1. Grossman VG, Bazarov BG, Bazarova ZhG. Subsolidus phase diagrams for the $Tl_2MoO_4$–$Ln_2(MoO_4)_3$–$Hf(MoO_4)_2$ systems, where Ln = La–Lu. *Russ J Inorg Chem.* 2008;53(11):1788–94. DOI:10.1134/S003602360811020X
2. Grossman VG, Bazarov BG, Klevtsova RF, Glinskaya LA, Bazarova ZhG. Phase equilibria in the $Tl_2MoO_4$–$Fe_2(MoO_4)_3$–$Hf(MoO_4)_2$ system and the crystal structure of ternary molybdate $Tl(FeHf_{0.5})(MoO_4)_3$. *Russ Chem Bull.* 2012;61(8):1546–9. DOI:10.1007/s11172-012-0202-7
3. Pleskov MY, Morozov VA, Lazoryak BI, Zhizhin MG, Burdakova IB, Khalbaeva KM, Tsyrenova GD, Khaikina EG. Structures of double molybdates $TlR(MoO_4)_2$ (R = In, Sc, Fe, Cr, Al). *Russ J Inorg Chem.* 2005(4);50:604–14.
4. Bazarov BG, Klevtsova RF, Bazarova TsT, Glinskaya LA, Fedorov KN, Bazarova ZhG, Chimitova OD. Systems $Tl_2MoO_4$–$E(MoO_4)_2$, where E = Zr or Hf, and the crystal structure of $Tl_8Hf(MoO_4)_6$. *Russ J Inorg Chem.* 2006;51(5):794–9. DOI:10.1134/S0036023606050184
5. Tushinova YuL, Bazarova ZhG, Archincheyeva SI. Abstracts of the reports. Ulan-Ude (Russia): Publishing house of BSC SB RAS; 2002. p. 90–1. Russian.
6. Bazarov BG, Klevtsova RF, Chimitova OD, Glinskaya LA, Fedorov KN, Tushinova YuL, Bazarova ZhG. Phase formation in the $Rb_2MoO_4$–$Er_2(MoO_4)_3$–$Hf(MoO_4)_2$ system and the crystal structure of new triple molybdate $Rb_5ErHf(MoO_4)_6$. *Russ J Inorg Chem.* 2006;51(5):800–4. DOI:10.1134/S0036023606050196
7. Shannon RD. Revised effective ionic radii and systematic studies of interatomic distances in halides and chalcogenides. *Acta Cryst.* 1976;A32:751–67. DOI:10.1107/S0567739476001551



**Cite this article as:**

Grossman VG, Bazarova BG, Bazarova ZhG. Phase equilibria in the $Tl_2MoO_4$–$R_2(MoO_4)_3$–$Zr(MoO_4)_2$ (R = Al, Cr) systems: synthesis, structure and properties of new triple molybdates $Tl_5RZr(MoO_4)_6$ and $TlRZr_{0.5}(MoO_4)_3$. *Chimica Techno Acta*. 2017;4(4):218–23. DOI:10.15826/chimtech/2017.4.4.02.

Bazarova Zh. G., Grossman V. G., Bazarov B. G.,
Tushinova Yu. L., Chimitova O. D., Bazarova Ts. T.
Chimica Techno Acta. 2017. Vol. 4, No. 4. P. 224–230.
ISSN 2409–5613

DOI: 10.15826/chimtech/2017.4.4.03

**Zh.G. Bazarova[1,2], V.G. Grossman[1], B.G. Bazarov[1,2], Yu.L. Tushinova[1,2], O.D. Chimitova[1], Ts.T. Bazarova[1]**

*[1]Baikal Institute of Nature Management, Siberian Branch of Russian Academy of Sciences, 8 Sakh'yanovoi St., Ulan-Ude, 670047, Russian Federation*
*[2]Buryat State University, 24a SmolinaSt., Ulan-Ude, 670000, Russian Federation*
*e-mail: jbaz@binm.ru*

# Phase diagrams for the $M_2MoO_4$–$Ln_2(MoO_4)_3$–$Hf(MoO_4)_2$ systems, where M = Li–Cs, Tl and Ln = La–Lu

In this paper, the results of systematic studies of complex molybdate systems $M_2MoO_4$–$Ln_2(MoO_4)_3$–$Hf(MoO_4)_2$ (M = Li–Cs, Tl; Ln = La–Lu) are presented. Subsolidus phase diagrams of ternary systems were constructed and new triple molybdates were obtained. The optimum synthesis conditions for poly- and monocrystalline form were determined. According to single-crystal data, the structure of one of the representatives of triple molybdates was determined.

**Keywords:** phase equilibria, synthesis, systems, lithium, sodium, potassium, rubidium, cesium, thallium, lanthanides, hafnium, crystal structure.

Received: 17.11.2017; accepted: 06.12.2017; published: 25.12.2017.



## Introduction

The molybdates containing tetrahedrally coordinated anions $MoO_4^{2-}$ are among the most exciting objects in inorganic and crystal chemistry. Special attention has been paid to the molybdates that include luminescent elements, such as Ce, Pr, Eu, Tb, Tm, in their composition. These compounds can be used as phosphors for white light emitting diodes. Currently, numerous studies had been undertaken that aim to search for new effective phosphors for the creation of WLED. These phosphors should possess high stability, compactness, high luminescence efficiency when excited by near UV, long lifetime and low cost. Luminescent materials containing rare-earth elements are also within the scope of such studies [1–3]. In this paper, we present results on the study of phase equilibria in ternary molybdate systems containing single-, three- and tetravalent elements, as well as data on the crystal structure of complex molybdate structural types.

## Experimental

Reagents $Li_2MoO_4$ ("pure" grade), $Na_2MoO_4{\cdot}2H_2O$ ("pure for analysis" grade), $K_2MoO_4$ ("pure" grade), $Cs_2MoO_4$ ("pure" grade), $Rb_2CO_3$ ("chemically pure" grade), $Tl_2O_3$ ("chemically pure" grade), $MoO_3$ ("chemically pure" grade), $HfO_2$ ("chemically pure" grade), and rare earth oxides of 99.9% purity

were used as starting materials. $Hf(MoO_4)_2$ and $Ln_2(MoO_4)_3$ were synthesized by the solid state method. The annealing had started at 400–500 °C with the following temperature increase up to 800 °C in order to prevent $MoO_3$ losses due to its high volatility. The total calcination time was 100–150 h. $Rb_2MoO_4$ was prepared within the temperature range 350–650 °C during 100 h. $Tl_2MoO_4$ was synthesized during 50 h firing starting at 400 °C with final temperature equal to 550 °C. The samples were regrinded after each 24 h in the course of annealing in order to reach better homogeneity.

The phase formation inside a subsolidus region of the ternary salt systems $M_2MoO_4$–$Ln_2(MoO_4)_3$–$Hf(MoO_4)_2$ (M = Li–Cs, Tl; Ln = La–Lu) in air were studied using the intersecting joins method. The phase composition of the samples was monitored by X-ray diffraction (XRD) measurements using Bruker D8 Advance diffractometer (Cu Kα radiation, VANTEC-1, maximum angle 2θ=100°, scan step 0.01–0.02°). Primary fitting of the diffraction patterns was made using PROFAN software from the CSD package.

## Results and discussion

The data concerning phase equilibrium for the side systems of studied triangles (quasi-ternary systems) $M_2MoO_4$–$Ln_2(MoO_4)_3$–$Hf(MoO_4)_2$ (M = Li–Cs, Tl; Ln = La–Lu) are taken from the literature. The phase formation in the quasi-binary $Li_2MoO_4$–$Ln_2(MoO_4)_3$ systems was described in paper [4] in details. The aforementioned systems can be divided into two groups. The first group includes systems with Ln = La–Tb in which two intermediate phases $LiLn_5(MoO_4)_8$ and $LiLn(MoO_4)_2$ possess a significant homogeneity range. The second group includes the systems with Ln = Dy–Lu. Inside these systems two intermediate compounds that did not exhibit any noticeable homogeneity ranges were detected: $LiLn(MoO_4)_2$ and $Li_7Ln_3(MoO_4)_8$.

Two intermediate compounds with the constituents mole ratio of 5:1 and 1:1 were detected inside the quasi-binary $Na_2MoO_4$–$Er_2(MoO_4)_3$ systems similarly to the $K_2MoO_4$–$Ln_2(MoO_4)_3$ (Ln = La, Tb, Dy, Er), $M_2MoO_4$–$Ln_2(MoO_4)_3$ (M = Tl, Rb; Ln = La–Lu) systems [4–8]. Additionally to those two one more intermediate phase with the constituents mole ratio 1:5 was found to exist inside the $Na_2MoO_4$–$Ln_2(MoO_4)_3$ (Ln = Nd, Sm) and $K_2MoO_4$–$Sm_2(MoO_4)_3$ systems [4, 5].

The phases formed inside the cesium-containing rare-earth molybdate systems included those with the constituents mole ratio 3:1 and 1:1 with Ln = Nd, whereas the systems with Ln = Sm, Tb, Er revealed only 1:1 compound [4, 5].

Lithium hafnium molybdate with the significant homogeneity range $Li_{10-4x}Hf_{2+x}(MoO_4)_9$ ($0.21 \le x \le 0.68$) was formed in the $Li_2MoO_4$–$Hf(MoO_4)_2$ system [9], but in the oxide systems with larger alkali earth metals $M_2MoO_4$–$Hf(MoO_4)_2$ (M = K, Tl, Rb, Cs) two types of compounds were confirmed – $M_8Hf(MoO_4)_6$ and $M_2Hf(MoO_4)_3$ [10–13]. It should be noted that Na-containing system slightly differs from the aforementioned ones. It was found that along with phases with the constituents mole ratios equal to 4:1 and 1:1 one more compound is formed with the 3:1 composition.

The phases that were isolated in the $Ln_2(MoO_4)_3$–$Hf(MoO_4)_2$ systems

are $Ln_2Hf_3(MoO_4)_9$ (Ln = La–Tb), $Ln_2Hf_2(MoO_4)_7$ (Ln = Sm–Ho), and $Ln_2Hf(MoO_4)_5$(Ln = Er–Lu) [14].

The phase diagrams for various molybdate systems are shown in Fig. 1–6, and the corresponding phase compositions are listed in Table 1.

No new compounds were detected in the lithium-containing and sodium-containing systems [15, 16]. In contrast, the new compounds listed in Table 1 and shown in Fig. 3–6 were confirmed in the $M_2MoO_4$–$Ln_2(MoO_4)_3$–$Hf(MoO_4)_2$ (M = K, Rb, Tl, Cs; Ln = La–Lu) systems [14, 17, 18].

The molybdates with the composition $K_5LnHf(MoO_4)_6$ were identified in the systems with Ln = Sm–Lu.

Two types of compounds, namely $M_5LnHf(MoO_4)_6$ (5:1:2) and $M_2LnHf_2(MoO_4)_{6.5}$ (2:1:4), were isolated in the $Tl_2MoO_4$–$Ln_2(MoO_4)_3$–$Hf(MoO_4)_2$ (Ln = Ce–Lu) and $Rb_2MoO_4$–$Ln_2(MoO_4)_3$–$Hf(MoO_4)_2$ (Ln = Ce–Lu) systems. In case of the Tl-containing systems, for Ln = Ce–Nd one more phase except those mentioned above had been obtained – $TlLnHf_{0.5}(MoO_4)_3$ (1:1:1).

The phase with composition $Cs_2LnHf_2(MoO_4)_{6.5}$ (2:1:4) was found to

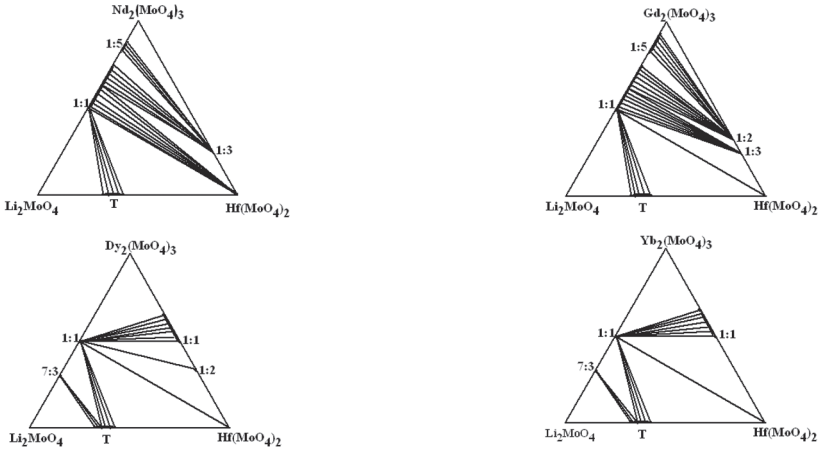


Fig. 1. Subsolidus phase diagrams of the $Li_2MoO_4$–$Ln_2(MoO_4)_3$–$Hf(MoO_4)_2$ systems ($T – Li_{10-4x}Hf_{2+x}(MoO_4)_9$, $0.21 \le x \le 0.68$; shaded double-phase equilibrium region) [15]

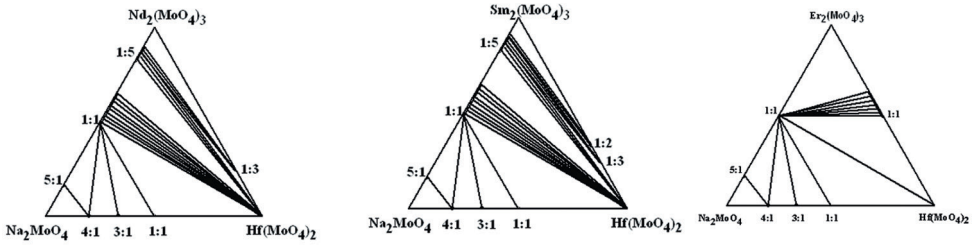


Fig. 2. Subsolidus phase diagrams of the $Na_2MoO_4$–$Ln_2(MoO_4)_3$–$Hf(MoO_4)_2$ systems; shaded double-phase equilibrium region [16]

exist in the Cs-containing rare earth molybdates with Ln = Pr–Lu.

The systems $M_2MoO_4$–$Ln_2(MoO_4)_3$–$Hf(MoO_4)_2$ (M = K, Rb, Tl, Cs; Ln = La–Lu) are characterized by the formation of a different number of phases with varying homogeneity ranges with respect to the lanthanide elements. One can see that $M_5LnHf(MoO_4)_6$ (M = K, Tl, Rb) compounds were formed if the size difference for the single charged $M^+$ cation and rare earth element cation $Ln^{3+}$ lies in the range of $0.682 \text{ Å} \le r(M^+)_{(CN=12)} - r(Ln^{3+})_{(CN=6)} \le 0.859$ Å [19]. In the case of $M^+ = Li^+$, $Na^+$, $Cs^+$ such radii difference lies outside this range. As a result, formation of $M_5LnHf(MoO_4)_6$ compounds for these cations is impossible.

If the size difference for the single charged $M^+$ cation and rare earth element cation $Ln^{3+}$ lies in the range $0.839 \text{ Å} \le r(M^+)_{(CN=12)} - r(Ln^{3+})_{(CN=6)} \le 1.019$ Å, it

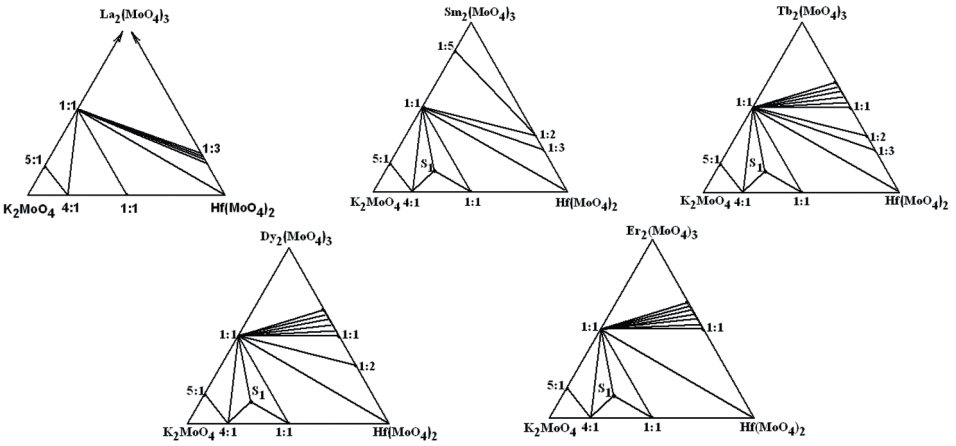


Fig. 3. Subsolidus phase relations in the $K_2MoO_4$–$Ln_2(MoO_4)_3$–$Hf(MoO_4)_2$ systems ($S_1$–$K_5LnHf(MoO_4)_6$ (5:1:2); shaded double-phase equilibrium region) [14]

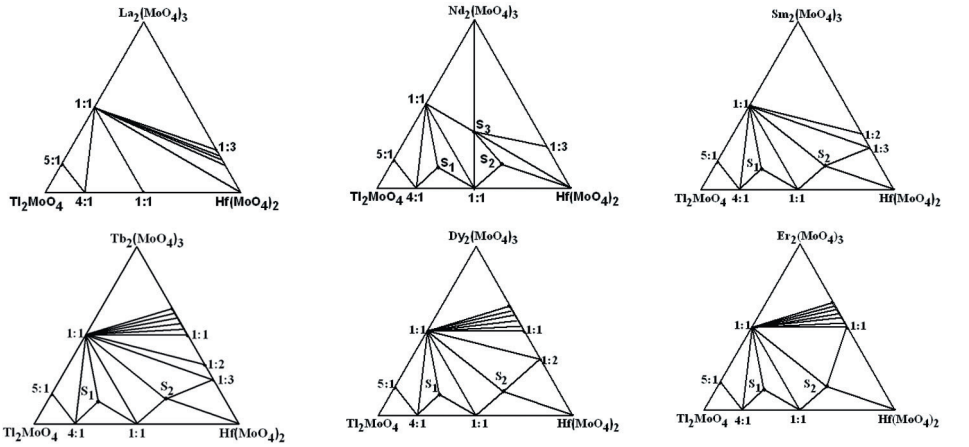


Fig. 4. Subsolidus phase diagrams for the $Tl_2MoO_4$–$Ln_2(MoO_4)_3$–$Hf(MoO_4)_2$ systems where Ln = La–Lu. Notations: $S_1$–$Tl_5LnHf(MoO_4)_6$ (5:1:2), $S_2$–$Tl_2LnHf_2(MoO_4)_{6.5}$ (2:1:4), and $S_3$–$TlLnHf_{0.5}(MoO_4)_3$ (1:1:1); shaded double-phase equilibrium region [17]

Table 1

Compositions of triple molybdates in the $M_2MoO_4$–$Ln_2(MoO_4)_3$–$Hf(MoO_4)_2$ (M = Li–Cs, Tl; Ln = La–Lu) systems

| | La | Ce | Pr | Nd | Sm | Eu | Gd | Tb | Dy | Ho | Er | Tm | Yb | Lu |
|---|---|---|---|---|---|---|---|---|---|---|---|---|---|---|
| LiHf | | | | | | | | | | | | | | |
| NaHf | | | | | | | | | | | | | | |
| KHf | | | | | $K_5LnHf(MoO_4)_6$ | | | | | | | | | |
| TlHf | | $Tl_5LnHf(MoO_4)_6$ | | | | | | | | | | | | |
| | | $Tl_2LnHf_2(MoO_4)_{6.5}$ | | | | | | | | | | | | |
| | | $TlLnHf_{0.5}(MoO_4)_3$ | | | | | | | | | | | | |
| RbHf | | $Rb_5LnHf(MoO_4)_6$ | | | | | | | | | | | | |
| | | $Rb_2LnHf_2(MoO_4)_{6.5}$ | | | | | | | | | | | | |
| CsHf | | | $Cs_2LnHf(MoO_4)_{6.5}$ | | | | | | | | | | | |

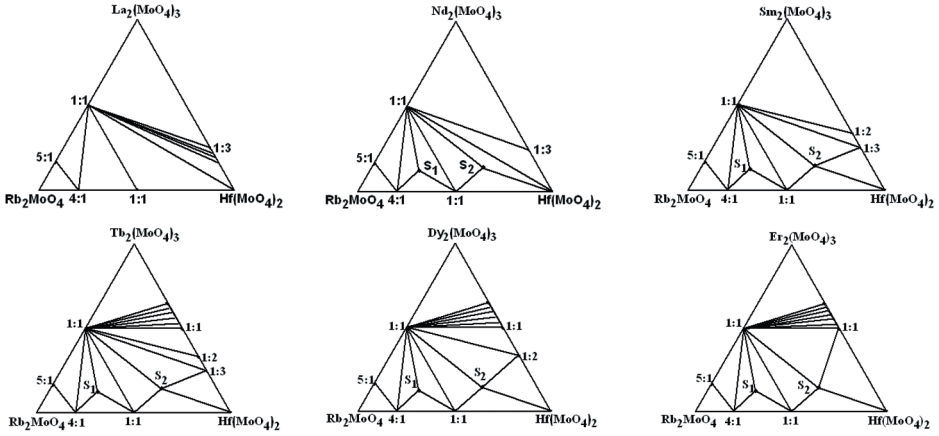


Fig. 5. Subsolidus phase diagrams for the $Rb_2MoO_4$–$Ln_2(MoO_4)_3$–$Hf(MoO_4)_2$ systems where Ln = La–Lu. Notations: $S_1$–$Rb_5LnHf(MoO_4)_6$ (5:1:2) and $S_2$–$Rb_2LnHf_2(MoO_4)_{6.5}$ (2:1:4); shaded double-phase equilibrium region [18]

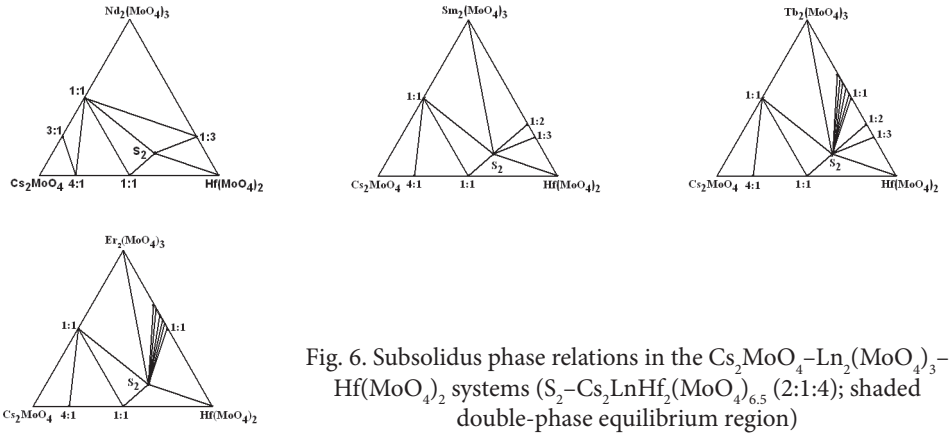


Fig. 6. Subsolidus phase relations in the $Cs_2MoO_4$–$Ln_2(MoO_4)_3$–$Hf(MoO_4)_2$ systems ($S_2$–$Cs_2LnHf_2(MoO_4)_{6.5}$ (2:1:4); shaded double-phase equilibrium region)

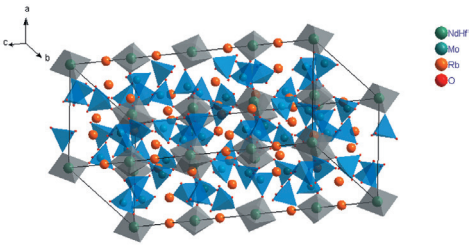


Fig. 7. Crystal structure fragment for $Rb_5NdHf(MoO_4)_6$

makes a formation of the $M_2LnHf_2(MoO_4)_{6.5}$ molybdates possible. The complex molybdates $M_5LnHf(MoO_4)_6$ (M = K, Tl, Rb) are isostructural to the earlier grown single crystals of $Rb_5LnHf(MoO_4)_6$ (Ln = Nd, Eu, Er), which possess the trigonal structure with $R\bar{3}c$ space group [18]. Three-dimensional framework of this structure is built of the consequently alternating $MoO_4$ tetrahedra and (Ln, Hf)$O_6$ octahedra linked with each other through the common O-vertices. One of the structural peculiarities for this class of compounds is a random distribution of $Ln^{3+}$ and $Hf^{4+}$ cations over two crystallographic sites with various distribution coefficients. Rubidium cations fill two types of large cavities in the framework, forming differently oriented channels of a large diameter. It gives good expectations for the fast ionic transport in such structures (Fig. 7).

Unfortunately, we have failed to prepare single crystals of $M_2LnHf_2(MoO_4)_{6.5}$ (2:1:4) and $TlLnHf_{0.5}(MoO_4)_3$ (1:1:1) in the condition used in the present work.

## Acknowledgements

This work was carried out according to the state assignment BINM SB RAS (project No. 0339-2016-0007.). This work was supported by the Comprehensive Program of Basic Research SB RAS No II.2 «Integration and Development» (project No. 0339-2015-0039).

## References

1. Haque M, Lee HI, Kim DK. Luminescent properties of $Eu^{3+}$-activated molybdate-based novel red-emitting phosphors for LEDs. *J Alloys Compd.* 2009;481:792–6. DOI:10.1016/j.jallcom.2009.03.083.
2. Haque M, Kim DK. Luminescent properties of $Eu^{3+}$ activated $MLa_2(MoO_4)_4$ based (M = Ba, Sr and Ca) novel red-emitting phosphors. *Mater Lett.* 2009;3:793–6. DOI:10.1016/j.matlet.2009.01.018.
3. Liang Y, Noh HM, Ran W, Park SH, Choi BC, Jeong JH, Kim KH. The design and synthesis of new double perovskite (Na, Li)YMg(W, Mo)$O_6$: $Eu^{3+}$ red phosphors for white light-emitting diodes. *J Alloys Compd.* 2017;716:56–64. DOI:10.1016/j.jallcom.2017.05.027.
4. Evdokimov AA, Efremov VA, Trunov VK, Kleyman IA, Tananaev IV. Soedineniya redkozemel'nykh elementov. Molibdaty, vol'framaty [Rare-earth elements' compounds. Molibdates, wolframates]. Moscow: Nauka; 1991. 267 p. Russian.
5. Trunov VK, Efremov VA, Velikodny Yu A. [Crystal chemistry and properties of double molybdates and tungstates.] Leningrad (USSR): Nauka; 1986. 173 p. Russian.
6. Basovich OM. [New phases in $M_2MoO_4$–$Ln_2(MoO_4)_3$ (M = Ag, Tl) and $Li_2MoO_4$–$M_2MoO_4$–$Ln_2(MoO_4)_3$ (M = K, Rb, Tl) systems] [dissertation]. Irkutsk (Russia); 2006. Russian.

7. Spitsyn VI, Trunov VK. [New data on double tungstates and molybdates of composition $MeLn(EO_4)_2$]. [*Reports of the Academy of Sciences of the USSR*]. 1969;185(4):854–5. Russian.
8. Savel'eva MV, Shakhno IV, Plyushchev VE. [Synthesis and properties of molybdates of alkaline and some rare-earth elements]. *Izv AN SSSR: Inorg Mat.* 1970;6(9):1665–9. Russian.
9. Solodovnikov SF, Balsanova LV, Bazarov BG, Zolotova ES, Bazarova Zh G. Phase formation in the $Rb_2MoO_4$–$Li_2MoO_4$–$Hf(MoO_4)_2$ system and the crystal structure of $Rb_5(Li_{1/3}Hf_{5/3})(MoO_4)_6$. *Russ J Inorg Chem.* 2003;48(7):1084–8.
10. Zolotova ES. [Synthesis and physico-chemical properties of double molybdates of alkali and tetravalent elements] [dissertation]. Novosibirsk (Russia); 1986. Russian.
11. Klevtsov PV, Zolotova ES, Glinskaya LA, Klevtsova RF. Synthesis, thermal stability and crystal structure of rubidium double molybdates with zirconium and hafnium. *Russ J Inorg Chem.* 1980;25(7):1844–50.
12. Bazarov BG, Bazarova TsT, Fedorov KN, Bazarova ZhG, Klevtsova RF, Glinskaya LA. Systems $Tl_2MoO_4$–$E(MoO_4)_2$ where E = Zr, Hf and crystal structure of $Tl_8Hf(MoO_4)_6$. *Russ J Inorg Chem.* 2006;51(5):794–9. DOI:10.1134/S0036023606050184.
13. Klevtsova RF, Antonova AA, Glinskaya LA. The crystal structure of $Cs_2Hf(MoO_4)_3$. *Crystallography.* 1980;25(1):161–4.
14. Romanova EYu. [New double and triple molybdates in the $Ln_2(MoO_4)_3$–$Hf(MoO_4)_2$ and $K_2MoO_4$–$Ln_2(MoO_4)_3$–$Hf(MoO_4)_2$ (Ln = La–Lu, Y) systems] [dissertation]. Irkutsk (Russia); 2007. Russian.
15. Grossman VG, Bazarov BG, Tushinova YuL, Bazarova Zh G. Phase equilibria in the $Li_2MoO_4$–$Ln_2(MoO_4)_3$–$Hf(MoO_4)_2$ (Ln = La–Lu) systems. *Russ J Inorg Chem.* 2015;51(4):351–4. DOI:10.1134/S0020168515030061.
16. Tushinova YuL, Bazarova TsT, Bazarov BG. [Phase relations in the $Na_2MoO_4$–$Ln_2(MoO_4)_3$–$Zr(MoO_4)_2$ (Ln = Nd, Sm, Er, Lu)]. *Vestnik buryatskogo gosudarstvennogo universiteta* [*Bulletin of Buryat State University*]. 2014;3:3–6. Russian.
17. Grossman VG, Bazarov BG, Bazarova Zh G. Subsolidus phase diagrams for the $Tl_2MoO_4$–$Ln_2(MoO_4)_3$–$Hf(MoO_4)_2$ systems, where Ln = La–Lu. *Russ J Inorg Chem.* 2008;53(11):1788–94. DOI:10.1134/S003602360811020X.
18. Chimitova OD. [Phase equilibrium, crystalline structures and electrical properties of new triple molybdates in the $Rb_2MoO_4$–$Ln_2(MoO_4)_3$–$Hf(MoO_4)_2$ (Ln = La–Lu) systems] [dissertation]. Krasnoyarsk (Russia); 2008. Russian.
19. Shannon RD. Revised effective ionic radii and systematic studies of interatomic distances in halides and chalcogenides. *Acta Cryst.* 1976; A32:751–67. DOI:10.1107/S0567739476001551.

**Cite this article as:**
Bazarova ZhG, Grossman VG, Bazarov BG, Tushinova YuL, Chimitova OD, Bazarova TsT. Phase diagrams for the $M_2MoO_4$–$Ln_2(MoO_4)_3$–$Hf(MoO_4)_2$ systems, where M = Li–Cs, Tl and Ln = La–Lu. *Chimica Techno Acta*. 2017;4(4):224–30. DOI:10.15826/chimtech/2017.4.4.03.

Koroleva M.S., Piir I.V., Istomina E.I.
Chimica Techno Acta. 2017. Vol. 4, No. 4. P. 231–241.
ISSN 2409–5613

DOI: 10.15826/chimtech/2017.4.4.04

**M.S. Koroleva, I.V. Piir, E.I. Istomina**

*Institute of Chemistry Komi SC UB RAS*
*48 Pervomayskaya St., Syktyvkar, 167982, Russian Federation*
*e-mail: marikorolevas@gmail.com*

# Synthesis, structure and electrical properties of Mg-, Ni-codoped bismuth niobates

Mg-, Ni-codoped bismuth niobates $Bi_{1.6}Mg_{0.8-x}Ni_xNb_{1.6}O_{7-\delta}$ ($x$ = 0; 0.2; 0.4; 0.6; 0.8) were obtained by conventional solid-state reaction method. It was shown that the Mg atoms are distributed at the Nb sites while the Ni atoms are distributed over the Bi- and the Nb-sites, according to the results of comparison of pycnometric and X-ray density of the $Bi_{1.6}Mg_{0.4}Ni_{0.4}Nb_{1.6}O_{7-\delta}$ pyrochlore. In this case, about 15–20% of the vacancies are formed at the Bi sites. The obtained compounds are stable up to their melting point based on the DSC analysis data. Real dielectric permittivity ε' of the $Bi_{1.6}Mg_{0.8-x}Ni_xNb_{1.6}O_{7-\delta}$ samples decreases from 80 to 65 with the temperature decrease from 25 to 700 °C and practically does not depend on frequency in the range of 1–1000 kHz. Oxides $Bi_{1.6}Mg_{0.8-x}Ni_xNb_{1.6}O_{7-\delta}$ behave like insulators up to 280 °C, their conductivity increases with temperature ($E_{a,dc}$ ≈ 1.3 eV, dc) and with the Ni content at a given temperature.

**Keywords:** pyrochlore; $Bi_{1.6}Mg_{0.8-x}Ni_xNb_{1.6}O_{7-\delta}$; dopant distribution; dielectric behavior; electrical conductivity.

Received: 14.11.2017; accepted: 12.12.2017; published: 25.12.2017.



## Introduction

Ceramics in the $Bi_2O_3$-$M_xO_y$-$Nb_2O_5$ ternary system are interesting from the perspective of their dielectric properties. The most attention has been paid to the Zn-, Mg-containing bismuth niobates, which possess high dielectric constant (170–180) and low dielectric loss (~$10^{-4}$) at 1 MHz (at room temperature) [1–9]. To search for the same properties Fe- [10], Mn- [11–12], Co- [13], Ni- [12, 14–15], Cu- [12] and the mixed Zn-M (M – Sr [16], Ca [16–17], Mn [16, 18], Ti [19–22], Sn [19, 22], Zr [19, 21–22], Ce [19,22], Gd [21], Ta [23], La [24]), Mg-M (M – Sr [25], Nd [26], Cu [27]) bismuth niobates and other ones were synthesized. The improved permittivity was achieved by Ti doping of the Nb sites in the pyrochlore structure [21–22] and by Cu doping in $Bi_{1.5}Cu_xMg_{1-x}Nb_{1.5}O_7$ ($x$ = 0.075) [27]. In most cases, doping leads to the permittivity decrease and to the tangent loss increase. However, electrical properties of several systems were investigated in the high temperature range (up to 700 °C) only in order to determine their conductivity mechanism [3, 9, 19–20, 27]. In our previous work [28–29] we have determined that the dielectric constant of the $Bi_{1.6}Cu_xMg_{0.8-x}Nb_{1.6}O_{7-\delta}$ pyrochlores behave

unusually passing through a maximum (250–350 °C) with temperature increasing. The value of the dielectric constant at the maximum is very high: ~$10^6$ (100 Hz). Second-type phase transition was found at 200 °C. To establish the reasons for such behavior, the distribution of doped metals in the cation (A–, B–sites) positions in the pyrochlore structure ($A_2B_2O_6O'$, the space group $Fd\bar{3}m$ (No 227)) was studied by X-ray diffraction pattern refinement (Rietveld analysis), and by comparison of pycnometric density with the calculated one. It has been determined that the electronegativity plays the crucial factor for the distribution of the Mg atoms in the Nb sites and the Cu atoms – in the Bi and the Nb sites in equal ratios. In any case, there are 10–15% of vacancies in the Bi sites. In accordance with the other systems' investigations, the vacancy concentration always remains at about 5–10% in the Bi sites in the pyrochlore structure [4, 10–11, 14, 30]. In this work we have a goal to determine a distribution of Ni and Mg dopants in the pyrochlore structure and investigate the temperature dependence of electrical properties of the $Bi_{1.6}Mg_{0.8-x}Ni_xNb_{1.6}O_{7-\delta}$.

## Experimental

Mixed bismuth niobates $Bi_{1.6}Mg_{0.8-x}Ni_xNb_{1.6}O_{7-\delta}$ ($x$ = 0; 0.2; 0.4; 0.6; 0.8) were prepared by a conventional solid state reaction method [31–32] from the oxides with high degree of purity (>99.9%): $Bi_2O_3$, NiO, MgO, $Nb_2O_5$. The oxides were weighted in an appropriate ratio ($Bi_2O_3$:MgO:NiO:$Nb_2O_5$ = 0.8:(0.8-$x$):$x$:0.8), grinded, pressed into pellets and calcined at 650 °C (8 h), 850 °C (6 h), 900 °C (6 h), 950 °C (12 h), 1000 °C (6 h), 1050 °C (12 h), 1070 (6 h), and 1100 °C (11 h) consequently in corundum crucibles. The annealing at 650 °C was carried out in order to avoid significant bismuth weight loss and the melting stage of $Bi_2O_3$ at 824 °C. As the temperature and duration of the calcination increased, the impurity phase content decreased. After each firing step, the pellets were regrinded for 30 min and repressed. The pellets' diameter and thickness varied from 12 to 14 mm and from 2.2 to 2.7 mm, respectively.

The phase composition of the samples was examined by powder X-ray diffraction method on a SHIMADZU XRD-6000 diffractometer using Cu Kα emission within the angle range 10–80° (the step – 0.05°). Distribution of nickel and magnesium atoms in the $Bi_{1.6}Mg_{0.4}Ni_{0.4}Nb_{1.6}O_{7-\delta}$ pyrochlore was determined by Rietveld analysis (FullProf software package [33]). Scanning electron microscopy (SEM) was carried out on a TESCAN VEGA 3 SBU microscope. The local composition of the samples was studied on polished pellets by energy dispersion spectroscopy (EDS). Differential scanning calorimetry (DSC) and thermogravimetric analysis (TG) of $Bi_{1.6}Mg_{0.4}Ni_{0.4}Nb_{1.6}O_{7-\delta}$ powder were carried out in the air in platinum crucibles with heating up to 1300 °C and a heating rate of 5 °C/min (NETZSCH STA 409 PC/PG). The electrical measurements were performed on the pellets, both sides of which were coated uniformly with a silver paste. Capacitance and dielectric loss tangent were measured by MT–4090 LCR meter in different gases (air, $p(O_2)$ = 0.21 atm and oxygen, $p(O_2)$ = 0.99 atm) at four frequencies (1, 10, 100, 200 kHz) in the temperature range of 25–750 °C. The impedance plots were measured by immittance meter E7-28 at 0.5 V in the temperature and frequency ranges 25–700 °C and 24 Hz – 10 MHz, respectively. The

electrical data were collected after 10 min after the thermal equilibrium was reached. The thermoelectric effect – Seebeck coefficient – was determined in the temperature range 130–330 °C in a temperature gradient of 30–40 °C across the material.

## Results and discussion

### Synthesis and Characterization

The XRD patterns of $Bi_{1.6}Mg_{0.8-x}Ni_xNb_{1.6}O_{7-\delta}$ ($0 \le x \le 0.8$) are shown in Fig. 1. The pyrochlore structure is formed for the $Bi_{1.6}Mg_{0.4}Ni_{0.4}Nb_{1.6}O_{7-\delta}$ composition only. The small amounts of second phases, identified as $MgNb_2O_6$ (*Pbcn* space group) and as $NiNb_2O_6$ (*Pbcn* space group), were found in the samples with $x = 0$; 0.2 and with $x = 0.6$; 0.8, respectively.

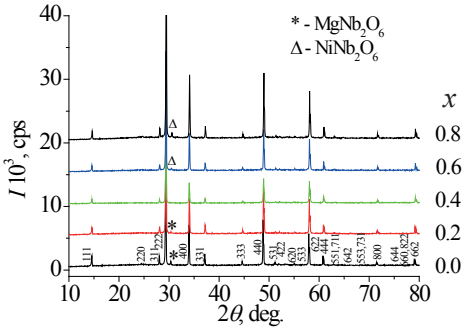


Fig. 1. X-ray diffraction patterns of $Bi_{1.6}Mg_{0.8-x}Ni_xNb_{1.6}O_{7-\delta}$ ($0 \le x \le 0.8$)

The surfaces of the $Bi_{1.6}Mg_{0.8-x}Ni_xNb_{1.6}O_{7-\delta}$ ($0 \le x \le 0.6$) polished pellets after the last calcination are shown in the SEM images (Fig. 2a–2c). According to the EDS data, the presence of additional phases such as $MgNb_2O_6$ (at $x = 0$) or as mixed Mg-Ni containing niobates (at $x = 0.2$; 0.6) can be seen. The amount of impurities is around 5%. The local compositions of the main and second phases are presented in the caption to Fig. 2. The composition of the $Bi_{1.6}Mg_{0.4}Ni_{0.4}Nb_{1.6}O_{7-\delta}$ ceramic determined by EDS is $Bi_{1.60}Mg_{0.38}Ni_{0.45}Nb_{1.6}O_{7-\delta}$, which is close to the desired composition. The porosity of the pellets was around 35–40%, as estimated from SEM micrographs.

DSC and TG curves of the $Bi_{1.6}Mg_{0.4}Ni_{0.4}Nb_{1.6}O_{7-\delta}$ powder are shown in Fig. 3. The endothermal effect was found on the DSC curve at 1261 °C. This effect may be associated with the melting of the sample. The reason for the weight rise during the heating process has not been established yet. It may be related to the partial oxidation of $Ni^{+2}$ to $Ni^{+3}$.

The Rietveld refinement of the XRD pattern of $Bi_{1.6}Mg_{0.4}Ni_{0.4}Nb_{1.6}O_{7-\delta}$ was carried out. The occupations of atom sites were fixed in accordance with the quantitative composition of the compound. The possibility of displacement of the bismuth atoms (from 16*c* sites to 96*h* or 96*g* sites) and the oxygen atoms O′ associated with bismuth (from 8*a* sites to 32*e* sites) were considered, like in $[Bi_{0.833}Mg_{0.11}\square_{0.04}]_2[Mg_{0.24}Nb_{0.76}]_2O_7$ and in $[Bi_{0.833}Ni_{0.125}\square_{0.04}]_2[Ni_{0.25}Nb_{0.75}]_2O_7$ pyrochlores [14]. Various models were studied to determine the distribution of doped atoms in the cation (Bi, Nb) sites of the pyrochlore structure. Among the alternative models that were considered there are $[Bi_{1.56}Ni_{0.34}\square_{0.10}][Ni_{0.05}Mg_{0.39}Nb_{1.56}]O_{7.02}$ and $[Bi_{1.56}Mg_{0.34}\square_{0.10}][Mg_{0.05}Ni_{0.39}Nb_{1.56}]O_{7.02}$. In these models 5% of vacancies remain at the Bi sites. The distribution of dopant atoms in equal ratio among two different cation sites causes formation of about 2.5% vacant sites both in the Bi and Nb sublattices. It is not typical for the pyrochlore structure. The best agreement between theoretical and observed X-ray patterns was obtained for the model designated as

$[Bi_{1.56}Ni_{0.34}\square_{0.10}][Ni_{0.05}Mg_{0.39}Nb_{1.56}]O_{7.02}$. In this model, all Mg atoms are distributed over the Nb sites. Several models were considered with different vacancy concentrations (10–25%) in the Bi sites and Mg atoms occupying the Nb sites.

The best values of $R_{wp}$ (%), $R_p$ (%), $\chi^2$ factors can be obtained for the models with 15–20% vacancies in the Bi sites. The refined crystallographic parameters of the $[Bi_{1.46}Ni_{0.18}\square_{0.36}][Ni_{0.18}Mg_{0.36}Nb_{1.46}]O_{6.52}$ model are presented in Table 1. This model corresponds to the equal distribution of Ni atoms in the Bi and the Nb sites, whereas 18% of vacancies remain in the Bi sites. Displacement of Bi and Ni atoms (16*c*

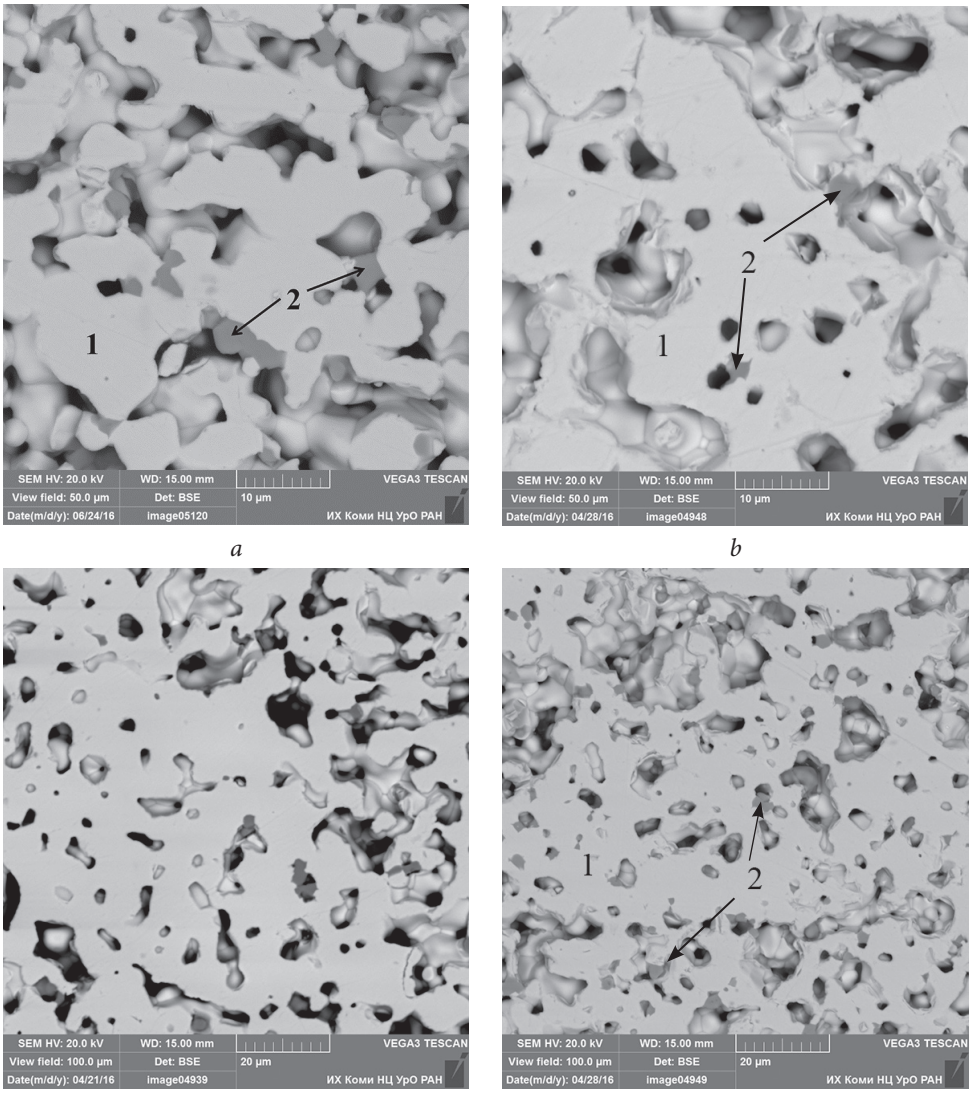


Fig. 2. SEM images of $Bi_{1.6}Mg_{0.8-x}Ni_xNb_{1.6}O_{7-\delta}$ samples: *a* – $x = 0$ (1 – $Bi_{1.72}Mg_{0.78}Nb_{1.6}O_{7-\delta}$, 2 – $MgNb_2O_6$); *b* – $x = 0.2$ (1 – $Bi_{1.60}Mg_{0.44}Ni_{0.18}Nb_{1.6}O_{7-\delta}$, 2 – $Mg_{0.85}Ni_{0.11}Nb_2O_6$); *c* – $x = 0.4$ ($Bi_{1.60}Mg_{0.38}Ni_{0.45}Nb_{1.6}O_{7-\delta}$); *d* – $x = 0.6$ (1 – $Bi_{1.68}Mg_{0.16}Ni_{0.56}Nb_{1.6}O_{7-\delta}$, 2 – $Mg_{0.35}Ni_{0.55}Nb_2O_6$)

to 96*h* sites) is observed. The observed, calculated and difference X-ray diffraction profiles for the model are shown in Fig. 4. To our mind, the distribution of dopant atoms in the cation sites is governed by the electronegativity values, apart from the ionic radii influence. So, $Mg^{2+}$ and $Ni^{2+}$ ionic radii are close (0.72 Å and 0.70 Å, respectively) [34]. The electronegativity of Mg (1.23) by Allred-Rochow [35] is equal to that of Nb (1.23), and the electronegativity of Ni (1.75) is close to that of Bi (1.67). Obviously, the electronegativity values impact on the dopant distribution in the pyrochlore structure, like in the Cu–Mg substituted bismuth niobates [28–29].

The pycnometric density of the $Bi_{1.6}Mg_{0.4}Ni_{0.4}Nb_{1.6}O_{7-\delta}$ powder is 6.50±0.24 g/cm³. The calculated density for the $[Bi_{1.56}M_{0.34}\square_{0.10}][M_{0.44}Nb_{1.56}]O_{7.02}$ model where M – the dopant metals (5% of vacancies in the Bi sites) is 7.02 g/cm³. The calculated density for the model with 18% vacancies in the Bi sites ($[Bi_{1.46}M_{0.18}\square_{0.36}][M_{0.54}Nb_{1.46}]O_{6.52}$) is 6.53 g/cm³ and is in agreement with the pycnometric density value. Thus assumed amount of about 15–20% vacant sites in Bi sublattice seems to be in agreement with the experimental results obtained in the present study.

**Electrical properties**

Complex impedance plots of the $Bi_{1.6}Mg_{0.8-x}Ni_xNb_{1.6}O_{7-\delta}$ ceramics were drawn from impedance spectroscopy data. The data were obtained during cooling from 700 to 160 °C to exclude proton conductivity. Perfect semicircles are traced in

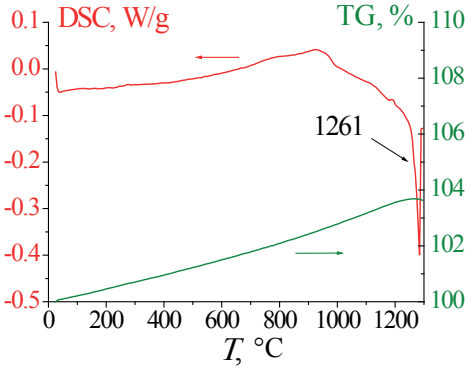


Fig. 3. DSC and TG curves of $Bi_{1.6}Mg_{0.4}Ni_{0.4}Nb_{1.6}O_{7-\delta}$

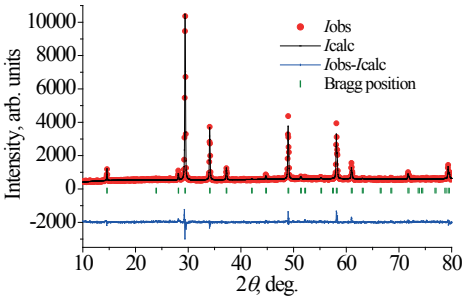


Fig. 4. Observed, calculated and difference X-ray diffraction profiles for $[Bi_{1.46}Ni_{0.18}\square_{0.36}][Ni_{0.18}Mg_{0.36}Nb_{1.46}]O_{6.52}$

Table 1

Refined crystallographic parameters for $Bi_{1.6}Mg_{0.4}Ni_{0.4}Nb_{1.6}O_{7-\delta}$ (space group *Fd*3*m*)

| Atom type | Site | *x* | *y* | *z* | $B_{iso}$, Å² | Occupation |
|---|---|---|---|---|---|---|
| $[Bi_{1.46}Ni_{0.18}\square_{0.36}][Ni_{0.18}Mg_{0.36}Nb_{1.46}]O_{6.52}$ | | | | | | |
| Bi/Ni | 96*h* | 0 | 0.015 | 0.985 | 0.708 | 0.725/0.09 |
| Nb/Ni | 16*d* | 1/2 | 1/2 | 1/2 | 0.003 | 0.725/0.09 |
| Nb/Mg | 16*d* | 1/2 | 1/2 | 1/2 | 0.003 | 0.725/0.18 |
| O | 48*f* | 1/8 | 1/8 | 0.428 | 0.010 | 1 |
| O' | 8*a* | 1/8 | 1/8 | 1/2 | 0.010 | 0.52 |

$a$ = 10.5204 Å; $R_p$ = 4.51%, $R_{wp}$ = 5.86%, $\chi^2$ = 2.22.

the temperature range 320–700 °C. At the temperature less than 320 °C half semicircles may be observed. In Fig. 5 impedance plots for the $Bi_{1.6}Mg_{0.8-x}Ni_xNb_{1.6}O_{7-\delta}$ ($x$ = 0.4; 0.6) ceramics are presented. The plots are well fitted by a single parallel RC element (inset of Fig. 5) where $R$ and $C$ belong to bulk resistance and capacitance, respectively [36–38]. The measured parameters are listed in Table 2.

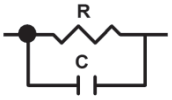


Permittivity recalculated from the capacitance values for the samples with Ni content $x$ = 0.20, 0.40, and 0.60 is (70–81), (70–81), and (65–76), respectively, for the temperature range of 700–280 °C. Calculated permittivity does not depend on the frequency in the range of 1–1000 kHz and is close to the dc permittivity values. At room temperature, the permittivity is around 80 in the frequency range of 1–1000 kHz. All ceramics under investigation behave like a dielectric ($\tan\delta \approx 0.002$) up to 280 °C.

Calculated from Arrhenius direct conductivity plots activation energy values are close to 1.2 eV (the third column in Table 3). These values are almost equal to ones at 1 kHz (the second column in Table 3). The corresponding Arrhenius con-

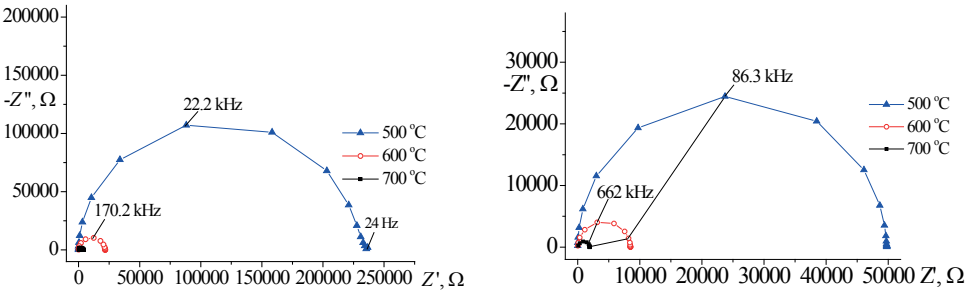


*a* *b*

Fig. 5. Complex impedance plots at 500, 600 and 700 °C for the $Bi_{1.6}Mg_{0.8-x}Ni_xNb_{1.6}O_{7-\delta}$ ceramics with $x$ = 0.4; 0.6

Table 2

$R_b$ and $C_b$ parameters of the RC elements in the temperature range 280–700 °C for the $Bi_{1.6}Mg_{0.8-x}Ni_xNb_{1.6}O_{7-\delta}$ ceramics

| $T$, °C | $x$ = 0.20 ($h$ = 0.265 cm; $d$ = 1.280 cm) | | $x$ = 0.40 ($h$ = 0.235 cm; $d$ = 1.300 cm) | | $x$ = 0.60 ($h$ = 0.220 cm; $d$ = 1.325 cm) | |
|---|---|---|---|---|---|---|
| | $R$, kΩ | $C$, pF | $R$, kΩ | $C$, pF | $R$, kΩ | $C$, pF |
| 280 | $(79\pm3)\cdot10^4$ | 34.77±0.08 | $(50\pm3)\cdot10^4$ | 40.61±0.18 | $(111.7\pm2.7)\cdot10^3$ | 42.03±0.26 |
| 320 | $(157.8\pm2.5)\cdot10^3$ | 34.32±0.11 | – | – | $(173\pm3)\cdot10^2$ | 41.4±0.3 |
| 360 | $(373\pm4)\cdot10^2$ | 33.99±0.15 | $(310\pm4)\cdot10^2$ | 39.77±0.20 | 2860±30 | 40.8±0.3 |
| 400 | 9420±60 | 33.57±0.14 | 7560±40 | 39.18±0.12 | 606.8±2.4 | 39.97±0.15 |
| 500 | 558.5±2.3 | 32.41±0.14 | 164.4±0.5 | 37.87±0.12 | 49.61±0.08 | 38.66±0.09 |
| 600 | 62.8±0.4 | 31.08±0.28 | 21.52±0.04 | 36.57±0.13 | 8.460±0.014 | 37.36±0.14 |
| 700 | 8.972±0.026 | 29.88±0.19 | 4.032±0.010 | 35.22±0.24 | 1.913±0.004 | 35.8±0.3 |

ductivity plots at 1 kHz for all ceramics are shown in Fig. 6a. The activation energy values, which are greater than 1 eV, may be associated with ionic conduction. The same activation energy values (~1.27 eV) are known for the $(Bi_{1.5}Zn_{0.5})(Nb_{0.5}M_{1.5})O_7$ (M – Ti, Sn, Zr, and Ce) ceramics [19] at $T > 350$ °C with the ionic type of conductivity.

The conductivity dependences on the temperature for the $Bi_{1.6}Mg_{0.4}Ni_{0.4}Nb_{1.6}O_{7-\delta}$ ceramic (160–750 °C) in the air and in the oxygen atmosphere are shown in Fig. 6b. The conductivity of the ceramic does not dependent on the oxygen pressure, and the value of Seebeck coefficient is near 0 mV/K in the temperature range of 200–340 °C. These data indicate that there is no impurity-caused conductivity.

For all ceramics, an electrical modulus ($M''$) maximum is detected on the logarithmic scale of frequency (Fig. 7), indicating the presence of a polarization process. These relaxation effects are characterized by the full width at half maximum (FWHM) peaks of $M''(f)$ being ~ 1.2 decades. This value is close to an ideal Debye response (1.14 decades) that characterizes the ceramics as electrically homogenous. At frequencies of the $M''$ maximum value the relaxation time was calculated (Fig. 7). Frequency values at $M''$ maxima were plotted vs temperature in an Arrhenius-type fashion. Obtained accordingly values of activation energy are

Table 3

Activation energies of (dc, ac) conductivity and relaxation process of the substituted bismuth niobate pyrochlores

| Compound | $E_a$ (conductivity, 1 kHz), eV | $E_a$ (conductivity, dc), eV | $E_a$ (relaxation), eV |
|---|---|---|---|
| $Bi_{1.6}Mg_{0.8}Nb_{1.6}O_{7-\delta}$ | 1.03±0.06 | – | – |
| $Bi_{1.6}Mg_{0.6}Ni_{0.2}Nb_{1.6}O_{7-\delta}$ | 1.09±0.03 | 1.25±0.03 | 1.38±0.03 |
| $Bi_{1.6}Mg_{0.4}Ni_{0.4}Nb_{1.6}O_{7-\delta}$ | 1.14±0.03 | 1.20±0.03 | 1.38±0.03 |
| $Bi_{1.6}Mg_{0.2}Ni_{0.6}Nb_{1.6}O_{7-\delta}$ | 1.10±0.03 | 1.20±0.04 | 1.23±0.04 |
| $Bi_{1.6}Ni_{0.8}Nb_{1.6}O_{7-\delta}$ | 1.17±0.08 | – | – |

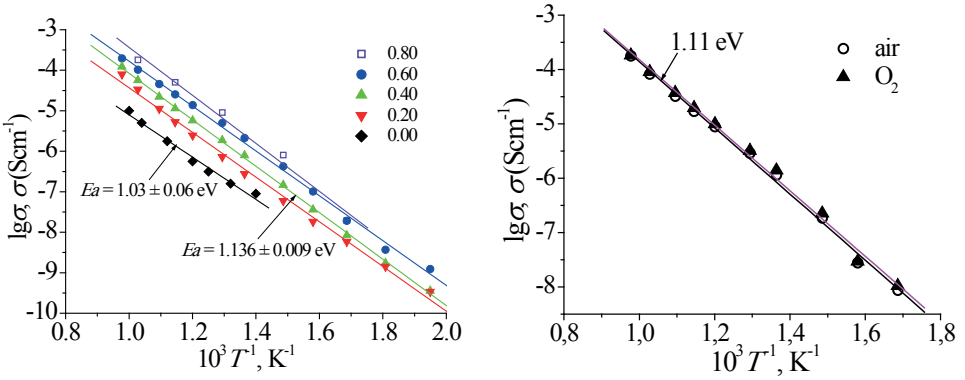


Fig. 6. Electrical conductivities as functions of reciprocal temperature at 1 kHz: *a* – $Bi_{1.6}Mg_{0.8-x}Ni_xNb_{1.6}O_{7-\delta}$; *b* – $Bi_{1.6}Mg_{0.4}Ni_{0.4}Nb_{1.6}O_{7-\delta}$

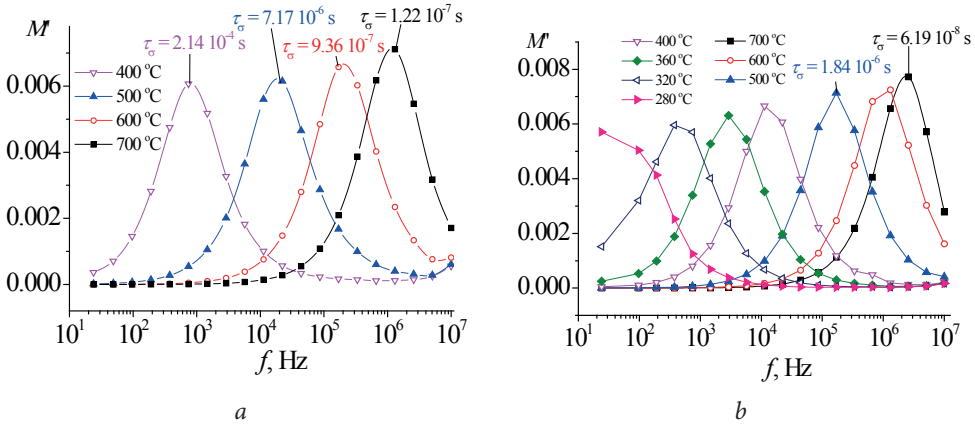


Fig. 7. Imaginary part of electrical modulus as a function of frequency for the $Bi_{1.6}Mg_{0.8-x}Ni_xNb_{1.6}O_{7-\delta}$ ceramics at $x = 0.4$ (*a*), $x = 0.6$ (*b*)

close to the ones obtained from the Arrhenius conductivity plots (Table 3). It points out that the hopping-type conductivity is typical for the $Bi_{1.6}Mg_{0.8-x}Ni_xNb_{1.6}O_{7-\delta}$ ceramics, like for $Bi_{1.5}ZnNb_{1.5}O_7$ [36, 38] and $Bi_{3.55}Mg_{1.78}Ta_{2.67}O_{13.78}$ [37] pyrochlores with $E_a$ (relaxation) are 0.94 eV and 1.37 eV, respectively.

## Conclusions

Mixed Mg–, Ni–containing bismuth niobates $Bi_{1.6}Mg_{0.8-x}Ni_xNb_{1.6}O_{7-\delta}$ ($0 \le x \le 0.8$) were synthesized by the conventional solid-state reaction method. For all samples the main crystal phase is the pyrochlore. The $Bi_{1.6}Mg_{0.4}Ni_{0.4}Nb_{1.6}O_{7-\delta}$ ceramic is a single-phase compound and is stable up to its melting point (1261 °C). Based on structural analysis and the comparison of pycnometric and calculated densities of the $Bi_{1.6}Mg_{0.4}Ni_{0.4}Nb_{1.6}O_{7-\delta}$, it was found that Mg atoms are distributed over the Nb sites, Ni atoms are distributed at the Bi and Nb sites almost in the equal ratio. In this case, there are about 15–20% vacant sites in the Bi sublattice. The $Bi_{1.6}Mg_{0.8-x}Ni_xNb_{1.6}O_{7-\delta}$ ceramics are characterized by the hopping type of conductivity ($E_a$ = 1.0–1.4 eV). It was determined that dielectric permittivity varies from 81 to 65 as the temperature increases from 280 to 700 °C, and practically does not depend on frequency in the range of 1–1000 kHz.


## Acknowledgements

This study received the financial support of Russian Foundation for Basic Research (project No. 15-03-09173 A). The study was performed using the equipment of the Center for Shared Use of Scientific Equipment "Khimiya" of the Institute of Chemistry, Komi Science Center, Ural Branch of the Russian Academy of Sciences.


## References


1. Nino JC, Lanagan MT, Randall CA. Dielectric Relaxation in $Bi_2O_3$–ZnO–$Nb_2O_5$ Cubic Pyrochlore. *J Appl Phys.* 2001;89(8):4512–6. DOI:10.1063/1.1357468.

2. Liu W, Wang H. Enhanced dielectric properties of $Bi_{1.5}ZnNb_{1.5}O_7$ thick films via cold isostatic pressing. *J Electroceram.* 2012;29:183–6. DOI:10.1007/s10832-012-9758-8.
3. Ren W, Trolier-Mckinstry S, Randall CA, Shrout TR. Bismuth zinc niobate pyrochlore dielectric thin films for capacitive applications. *J Appl Phys.* 2001;89(1):767–74. DOI:10.1063/1.1328408.
4. Levin I, Amos TG, Nino JC, Vanderah TA, Randall CA, Lanagan MT. Structural Study of an Unusual Cubic Pyrochlore $Bi_{1.5}Zn_{0.92}Nb_{1.5}O_{6.92}$. *J Solid State Chem.* 2002:168:69–75. DOI:10.1006/jssc.2002.9681.
5. Jiang SW, Li YR, Li RG, Xiong ND, Tan LF, Liu XZ, Tao BW. Dielectric properties and tunability of cubic pyrochlore $Bi_{1.5}MgNb_{1.5}O_7$ thin films. *Appl Phys Lett.* 2009;94:162908-1-162908-3. DOI:10.1063/1.3126442.
6. Xia W, Xue P, Wu H, Lu Y, Zhang Y, Zhou Sh, Zhu X. Dielectric properties and atomic-scale microstructural characterizations of cubic-pyrochlored ceramics in the system of $Bi_2O_3$-MgO-$Nb_2O_5$. *J Alloys Compd.* 2017;701:682-8. doi:10.1016/j.jallcom.2017.01.153.
7. Gao L, Jiang Sh, Li R, Li B, Li Y. Structure and dielectric properties of sputtered bismuth magnesium niobate thin films. *Thin Solid Films.* 2012;520:6295-8. DOI:10.1016/j.tsf.2012.06.035.
8. Zhang Y, Zhu X, Zhou Sh, Zhu J, Liu Zh, Al-Kassab T. Atomic-scale microstructural characterization and dielectric properties of crystalline cubic pyrochlore $Bi_{1.5}MgNb_{1.5}O_7$ nanoparticles synthesized by sol–gel method. *J Nanopart Res.* 2014;16:2208. DOI:10.1007/s11051-013-2208-y.
9. Tan PY, Tan KB, Khaw CC, Zainal Z, Chen SK, Chon MP. Phase equilibria and dielectric properties of $Bi_{3+(5/2)x}Mg_{2-x}Nb_{3-(3/2)x}O_{14-x}$ cubic pyrochlores. *Ceramics International.* 2014;40:4237–46. DOI:10.1016/j.ceramint.2013.08.087.
10. Lufaso MW, Vanderah TA, Pazos IM, Levin I, Roth RS, Nino JC, Provenzano V, Schenck PK. Phase formation, crystal chemistry, and properties in the system $Bi_2O_3$–$Fe_2O_3$–$Nb_2O_5$. *J Solid State Chem.* 2006;179:3900–10. DOI:10.1016/j.jssc.2006.08.036.
11. Vanderah TA, Lufaso MW, Adler AU, Levin I, Nino JC, Provenzano V, Schenck PK. Subsolidus phase equilibria and properties in the system $Bi_2O_3$:$Mn_2O_{3\pm x}$:$Nb_2O_5$. *J Solid State Chem.* 2006;179:3467-3477. DOI: 10.1016/j.jssc.2006.07.014.
12. Sirotinkin VP, Bush AA. Preparation and Dielectric Properties of $Bi_{1.5}MNb_{1.5}O_7$ (M = Cu, Mg, Mn, Ni, Zn) Pyrochlore Oxides. *Inorg Mater.* 2003;39(9):974–7. DOI:10.1023/A:1025517507623.
13. Vanderah TA, Siegrist T, Lufaso MW, Yeager MC, Roth RS, Nino JC, Yates S. Phase formation and properties in the system $Bi_2O_3$: $2CoO_{1+x}$:$Nb_2O_5$. *Eur J Inorg Chem.* 2006;23:4908–14. DOI:10.1002/ejic.200600661.
14. Nguyen HB, Norẻn L, Liu Y, Withers RL, Wei X, Elcombe MM. The disordered structures and low temperature dielectric relaxation properties of two misplaced-displacive cubic pyrochlores found in the $Bi_2O_3$–$M^{II}O$–$Nb_2O_5$ (M = Mg, Ni) systems. *J Solid State Chem.* 2007;180:2558–65. DOI:10.1016/j.jssc.2007.07.003.

15. Nguyen B, Liu Y, Withers RL. The local crystal chemistry and dielectric properties of the cubic pyrochlore phase in the $Bi_2O_3$–$M^{2+}O$–$Nb_2O_5$ ($M^{2+}$ – $Ni^{2+}$ and $Mg^{2+}$) systems. *J Solid State Chem.* 2007;180:549–57. DOI:10.1016/j.jssc.2006.10.039.
16. Li LX, Zhang S, Lv XS. Crystal chemistry and dielectric properties of $(Bi_{1.5}Zn_{0.4}M_{0.1})(Nb_{1.5}Zn_{0.5})O_7$ (M = Sr, Ca, Mn, Zn) pyrochlore oxides. *J Mater Sci: Mater Electron.* 2017;28(5):4388-95. DOI:10.1007/s10854-016-6066-0.
17. Shihua D, Yong P, Tianxiu S, Hongni W, Peng X, Lihua Y. Dielectric Properties of Ca Doping a-BZN Ceramics. *Ferroelectrics.* 2015;487:161–7. DOI:10.1080/00150193.2015.1071628
18. Luo W, Li L, Guo Q, Lv X. Crystal structure and dielectric properties of Mn-substituted $Bi_{1.5}Zn_{1.0}Nb_{1.5}O_7$ pyrochlore ceramics as temperature stable LTCC material. *J Mater Sci: Mater Electron.* 2017;28:5623–7. DOI:10.1007/s10854-016-6232-4.
19. Du H, Shi X, Cui Y. Defect structure and electrical conduction behavior of Bi-based pyrochlores. *Solid State Commun.* 2010;150:1213–6. DOI:10.1016/j.ssc.2010.04.008.
20. Osman RAM, West AR. Electrical characterization and equivalent circuit analysis of $(Bi_{1.5}Zn_{0.5})(Nb_{0.5}Ti_{1.5})O_7$ Pyrochlore, a relaxor ceramic. *J Appl Phys.* 2011;109:074106-1-074106-8. DOI:10.1063/1.3553883.
21. Valant M, Davies PK. Crystal Chemistry and Dielectric Properties of Chemically Substituted $(Bi_{1.5}Zn_{1.0}Nb_{1.5})O_7$ and $Bi_2(Zn_{2/3}Nb_{4/3})O_7$ Pyrochlores. *J Am Ceram Soc.* 2000;83(1):147–53. DOI:10.1111/j.1151-2916.2000.tb01163.x.
22. Du H, Yao X, Wang H. Dielectric properties of pyrochlore $(Bi_{1.5}Zn_{0.5})(Nb_{0.5}M_{1.5})O_7$ (M = Ti, Sn, Zr, and Ce) dielectrics. *Appl Phys Lett.* 2006;88:212901-1-212901-3. DOI:10.1063/1.2200480.
23. Qasrawi AF, Mergen A. Structural, electrical and dielectric properties of $Bi_{1.5}Zn_{0.92}Nb_{1.5-x}Ta_xO_{6.92}$ pyrochlore ceramics. *Ceramics International.* 2012;38:581–7. DOI:10.1016/j.ceramint.2011.07.046.
24. Wang H, Zhang D, Wang X, Yao X. Effect of $La_2O_3$ Substitution on Structure and Dielectric Properties of $Bi_2O_3$–ZnO–$Nb_2O_5$-based Pyrochlore Ceramics. *J Mater Res.* 1999;14(2):546–8. DOI:10.1557/JMR.1999.0078.
25. Dasin NAM, Tan KB, Khaw CC, Zainal Z, Chen SK. Subsolidus solution and electrical properties of Sr-substituted bismuth magnesium niobate pyrochlores. *Ceramics International.* 2017;43:10183–91. DOI:10.1016/j.ceramint.2017.05.043.
26. Huang B, Liu Y, Lu Y, Gao H, Chen H. Structure and dielectric properties of Nd substituted $Bi_{1.5}MgNb_{1.5}O_7$ ceramics. *J Mater Sci: Mater Electron.* 2013;24:2785–9. DOI:10.1007/s10854-013-1171-9.
27. Ning P-F, Li L-X, Xia W-S, Zhang X-Y. Low temperature crystallized voltage tunable $Bi_{1.5}Cu_xMg_{1-x}Nb_{1.5}O_7$ thin films capable of integration with Au electrode. *Ceramics International.* 2012;38:5299–303. DOI:10.1016/j.ceramint.2012.02.088.
28. Koroleva MS, Piir IV, Sekushin NA. Mg-Ni and Mg-Cu containing bismuth niobates: synthesis, structure and electrical properties. In: Articles of the 21h International Conference Solid State Ionics; 2017 June 18-23; Padua, Italy. p. 357.
29. Koroleva MS, Piir IV, Sekushin NA, Istomina EI. Sintez i elektricheskie svoystva magniy-med'-, magniy-nikel'soderzhashchikh niobatov vismuta [Synthesis and electrical properties of magnesium-copper, magnesium-nickel-containing bismuth

niobates]. In: Articles of the First International Conference on Intellect-intensive technologies in power engineering (physical chemistry and electrochemistry of molten and solid state electrolytes); 2017 Sep 18-22; Ekaterinburg, Russia. P. 363–365. Russian.
30. Withers RL, Welberry TR, Larsson A-K, Liu Y, Norén L, Rundlöf H, Brink FJ. Local crystal chemistry, induced strain and short range order in the cubic pyrochlore $(Bi_{1.5-\alpha}Zn_{0.5-\beta})(Zn_{0.5-\gamma}Nb_{1.5-\delta})O_{(7-1.5\alpha-\beta-\gamma-2.5\delta)}$ (BZN). *J Solid State Chem.* 2004;177(1):231–44. DOI:10.1016/j.jssc.2003.07.005
31. Piir IV, Koroleva MS, Ryabkov YuI, Pikalova EYu, Nekipelov SV, Sivkov VN, Vyalikh DV. Chemistry, structure and properties of bismuth copper titanate pyrochlores. *Solid State Ionics.* 2014;262:630–5. DOI:10.1016/j.ssi.2013.08.041.
32. Krasnov AG, Piir IV, Koroleva MS, Sekushin NA, Ryabkov YI, Piskaykina MM, Sadykov VA, Sadovskaya EM, Pelipenko VV, Eremeev NF. The conductivity and ionic transport of doped bismuth titanate pyrochlore $Bi_{1.6}M_xTi_2O_{7-\delta}$ (M – Mg, Sc, Cu). *Solid State Ionics.* 2017;302:118–25. DOI:10.1016/j.ssi.2016.12.019.
33. Rodríguez-Carvajal J. Recent advances inmagnetic structure determination by neutron powder diffraction. *Phys B Condens Matter.* 1993;192:55–69. DOI:10.1016/0921-4526(93)90108-I.
34. Shannon RD. Revised effective ionic radii and systematic studies of interatomic distances in halides and chalcogenides. *Acta Cryst.* 1976;A32:751–67. DOI:10.1107/S0567739476001551.
35. Allred AL, Rochow EG. A scale of electronegativity based on electrostatic force. *J Inorg Nucl Chem.* 1958;5(4):264–8. DOI:10.1016/0022-1902(58)80003-2.
36. Singh J, Krupanidhi SB. Probing disorder in cubic pyrochlore $Bi_{1.5}Zn_{1.0}Nb_{1.5}O_7$ (BZN) thin films. *Solid State Commun.* 2010;150:2257–61. DOI:10.1016/j.ssc.2010.09.030.
37. Tan PY, Tan KB, Khaw CC, Zainal Z, Chen SK, Chon MP. Structural and electrical properties of bismuth magnesium tantalate pyrochlores. *Ceramics International.* 2012;38(7):5401-9. DOI:10.1016/j.ceramint.2012.03.050.
38. Tan KB, Khaw CC, Lee CK, Zainal Z, Tan YP, Shaari H. High temperature impedance spectroscopy study of non-stoichiometric bismuth zinc niobate pyrochlore. *Mater Sci Pol.* 2009;27:947–59. Available from: http://www.materialsscience.pwr.wroc.pl/

**Cite this article as:**
Koroleva MS, Piir IV, Istomina EI. Synthesis, structure and electrical properties of Mg-, Ni-codoped bismuth niobates. *Chimica Techno Acta*. 2017;4(4):231–41. DOI:10.15826/chimtech/2017.4.4.04.

*Please note that all new submissions will be accepted in English only. Requirements for the manuscript preparation are available on the Journal's website and in the following template*

# Chimica Techno Acta manusctipt style guidelines (title)

A.N. Authorname[a], A.N. Authorname[b], A.N. Authorname[ab]
a Institution, address, city, country
b Institution, address, city, country
e-mail: corresponding_author@e-mail.com

**Abstract**

The abstract should be a single paragraph (up to 300 words) in plain text (that means – no formulae or references are permitted) that summarises the content of the article. It should set the main objectives and results of the work; giving the reader a clear idea of what has been achieved. An abstract should not be extremely short though – if yours is 1–2 sentences long, then you're not doing it right. Make sure that you use well-known, searchable terms and phrases.

**Keywords:** short; searchable; keywords (up to 10).

## Introduction

An introduction should 'set the scene' of the work. It should clearly explain both the nature of the problem under investigation and its background. It should start off general and then focus in to the specific research question you are investigating. Ensure you include all relevant references.

## **Experimental** (if appropiate)

Descriptions of the experiments should be provided in enough detail so that a skilled researcher is able to repeat them. Methods already published or experimental techniques already described elsewhere should be indicated by a reference. Only non-standard apparatus should be described in details; commercially available instruments are referred to by their stock numbers.

## Results and discussion

This is undoubtedly the most important section of your article. It should consist of the logically ordered sequence of text, formulae, images and tables.

All formulae which appear in their own line should be numbered:

$$A = B + C \tag{1}$$

Tables should be used only when they can present information more efficiently than running text or even an image:

Table 1

Just an ordinary table without any sophisticated formatting applied

| A | B | C | D |
|---|---|---|---|
| 1 | 2 | 3 | 4 |
| + | + | + | - |

All illustrations should be of a high quality (300 dpi or higher) and should be placed in the flow of the text, not in the end of an article:


Fig. 1. Just an ordinary image

Please bear in mind that all illustrations and tables should fit smoothly within either single column (approx. 6 cm) or double column (approx. 12 cm) width.

**Conclusions**

Your conclusions should summarize the main paper, underline the interpretation of the key results and highlight the novelty and significance of the work. They may address some plans for relevant future work as well.

**Acknowledgements** (if appropiate)

All sources of funding such as grants should be declared here. Individuals who contributed to the research but are not co-authors may also be briefly acknowledged.

**References**

A reference should be indicated in square brackets in line with the text (e.g. [1]). The actual references in the reference list should be numbered in the order in which they appear in the text. In Chimica Techno Acta so-called Vancouver Citation Style is adopted almost as it is described in the following public domain textbook [1]:

1. Patrias K. Citing medicine: the NLM style guide for authors, editors, and publishers [Internet]. 2nd ed. Wendling DL, technical editor. Bethesda (MD): National Library of Medicine (US); 2007- [updated 2015 Oct 2; cited 2017 Jun 07]. Available from: http://www.nlm.nih.gov/citingmedicine

Note that opposed to [1] we omit the date of publication (leaving year only) of the referenced journal article, as almost all journals are continuously paginated throughout the volume. And another one – DOI or a hyperlink should always come last in a reference. These are the only major differences between our style and such described in [1], so when in doubt – you can always refer to [1], it contains tremendous number of well-organized examples.

For your convenience, below are some references to the different types of publications:

**Books**

2. Livingstone S. The Chemistry of Ruthenium, Rhodium, Palladium, Osmium, Iridium and Platinum. Oxford: Pergamon; 1973. 222 p.

3. Bard AJ, Faulkner LR. Electrochemical Methods: Fundamentals and Applications. 2nd ed. New York: John Wiley & Sons; 2001. 833 p.

**Books not in English**

4. Evdokimov AA, Efremov VA, Trunov VK, Kleyman IA, Tananaev IV. Soedineniya redkozemel'nykh elementov. Molibdaty, vol'framaty [Rare-earth elements' compounds. Molibdates, wolframates]. Moscow: Nauka; 1991. 267 p. Russian.

* Translation of the title in square brackets is not required, but highly desirable.

* For Cyrillic languages, such as Russian, please use consistent transliteration system. There are plenty, but we strongly recommend BGN/PCGN Romanization as it's one of the

easiest to read and implement (https://en.wikipedia.org/wiki/BGN/PCGN_romanization_of_Russian).

**Journal articles**

5. Zuev AYu, Tsvetkov DS. Oxygen nonstoichiometry, defect structure and defect-induced expansion of undoped perovskite $LaMnO_{3\pm\delta}$. Solid State Ionics. 2010;81(11–12):557–63. DOI:10.1016/j.ssi.2010.02.024

6. Shannon RD. Revised effective ionic radii and systematic studies of interatomic distances in halides and chalcogenides. Acta Cryst. 1976;A32:751–67. DOI:10.1107/S0567739476001551

7. Allred AL, Rochow EG. A scale of electronegativity based on electrostatic force. J Inorg Nucl Chem. 1958;5(4):264–8. DOI:10.1016/0022-1902(58)80003-2

* For the majority of chemical journals corresponding abbreviation is defined in Chemical Abstracts Service Source Index (CASSI, http://cassi.cas.org). If an abbreviation is not available there, please use the full name of a journal.

* Note that DOI of an article, when available, should always be provided.

**Journal articles on the Internet** (e.g. for online-only journals without DOI)

8. Tkach V, Nechyporuk V, Yagodynets P. Descripción matemática de la síntesis electroquímica de polímeros conductores en la presencia de surfactants. Avances en Química [Internet]. 2013[cited 2016];8(1):9–15. Spanish. Available from: http://erevistas.saber.ula.ve/index.php/avancesenquimica/article/download/6357/6168

**Conference abstracts**

9. Zuev AYu, Sereda VV, Malyshkin DA, Ivanov IL, Tsvetkov DS. Mechano-chemical coupling in double perovskites as energy related materials. In: Abstracts of the XX Mendeleev Congress on general and applied chemistry, Vol. 3; 2016 Sep 26–30; Ekaterinburg, Russia. p. 325.

10. Steparuk AS, Usachev SA, Tsvetkov DS, Sosnovskikh VYa, Zuev AYu. Novyy katodnyy material na osnove mayenita dlya elektrokhimicheskogo karboksilirovaniya organicheskikh soedineniy [New mayenite-based cathode material for electrochemical carboxylation of organic compounds]. In: Tezisy dokladov XXVI Rossiyskoy molodezhnoy nauchnoy konferentsii "Problemy teoreticheskoy i eksperimental'noy khimii" [Abstracts of XXVI Russian scientific conference for young scientists "Problems of theoretical and experimental chemistry"]; 2016 Apr 27–29; Ekaterinburg, Russia. p. 285–286. Russian.

**Dissertations**

11. ten Donkelaar SFP. Development of Stable Oxygen Transport Membranes [dissertation]. Enschede (The Netherlands): University of Twente; 2015. 140 p.

**Patents**

12. Chemezov OV, Batukhtin VP, Apisarov AP, Isakov AV, Zaikov YuP, inventors; Institute of High-Temperature Electrochemistry UB RAS, assignee. Sposob polucheniya nano- i mikrovolokon kremniya elektrolizom dioksida kremniya iz rasplavov soley. Russian Federation patent RU 2427526. 2011 Aug 27. Russian.

13. Menta E, Da Re G, Grugni M., authors; Cti Europe S.R.L., assignee. Derivatives of chromen-2-one as inhibitors of vegf production in mammalian cells. United States patent US20060122387 A1. 2006 Jun 8.

*Chimica Techno Acta*




Учредитель – Уральский федеральный университет имени первого Президента России Б. Н. Ельцина
620002, Россия, Екатеринбург, ул. Мира, 19

Редактор *Е. Е. Крамаревская*
Художник-оформитель *Е. Р. Даурова*
Верстальщик *В. К. Матвеев*

Свидетельство о регистрации
ПИ № ФС77-56172 от 15.11.2013

Адрес журнала:
Россия, 620000,
Екатеринбург, ул. Мира, 28, оф. Х-268
E-mail: t.a.pospelova@urfu.ru
Формат 70×100/16. Заказ № ___.
Тираж 500 экз.
Отпечатано в типографии
Издательско-полиграфического центра УрФУ
620000, Екатеринбург, ул. Тургенева, 4
Тел.: +7 (343) 350-56-64, 350-90-13
Факс: +7 (343) 358-93-06
E-mail: press-urfu@mail.ru

Founded by Ural Federal University named after
the first President of Russia B. N. Yeltsin
19, Mira St., Ekaterinburg, 620002, Russia

Journal Registration Certificate
PI № FS 77-56172 as of 15.11.2013

Principal Contact
Office X-268, Mira Str.,
620000, Ekaterinburg, Russia
E-mail: t.a.pospelova@urfu.ru

Format 70×100/16.
Circulation 500 cop.

Publisher – Ural Federal University
Publishing Centre
4, Turgenev St., 620000 Ekaterinburg, Russia
Phone: +7 343 350 56 64, +7 343 350 90 13
Fax: +7 343 358 93 06
E-mail: press-urfu@mail.ru